


Scalable Circuits for Preparing Ground States on Digital Quantum Computers: The Schwinger Model Vacuum on 100 Qubits

Roland C. Farrell^{✉,*}, Marc Illa^{✉,†}, Anthony N. Ciavarella^{✉,‡} and Martin J. Savage^{✉,§}
*InQubator for Quantum Simulation (IQUS), Department of Physics, University of Washington, Seattle,
 Washington 98195, USA*

 (Received 8 September 2023; revised 12 December 2023; accepted 21 March 2024; published 18 April 2024)

The vacuum of the lattice Schwinger model is prepared on up to 100 qubits of IBM’s Eagle-processor quantum computers. A new algorithm to prepare the ground state of a gapped translationally invariant system on a quantum computer is presented, which we call “scalable circuits ADAPT-VQE” (SC-ADAPT-VQE). This algorithm uses the exponential decay of correlations between distant regions of the ground state, together with ADAPT-VQE, to construct quantum circuits for state preparation that can be scaled to arbitrarily large systems. These scalable circuits can be determined with use of classical computers, avoiding the challenging task of optimizing parameterized circuits on a quantum computer. SC-ADAPT-VQE is applied to the Schwinger model, and is shown to be systematically improvable, with an accuracy that converges exponentially with circuit depth. Both the structure of the circuits and the deviations of prepared wave functions are found to become independent of the number of spatial sites, L . This allows a controlled extrapolation of the circuits, determined with use of small or modest-sized systems, to arbitrarily large L . The circuits for the Schwinger model are determined on lattices up to $L = 14$ (28 qubits) with the Qiskit classical simulator, and are subsequently scaled up to prepare the $L = 50$ (100 qubits) vacuum on IBM’s 127-superconducting-qubit quantum computers `ibm_brisbane` and `ibm_cusco`. After introduction of an improved error-mitigation technique, which we call “operator decoherence renormalization”, the chiral condensate and charge-charge correlators obtained from the quantum computers are found to be in good agreement with classical matrix product state simulations.

DOI: [10.1103/PRXQuantum.5.020315](https://doi.org/10.1103/PRXQuantum.5.020315)

I. INTRODUCTION

Quantum simulations of physical systems described by the Standard Model [1–6], and descendant effective field theories, are anticipated to provide qualitatively new predictions about matter under extreme conditions; from the dynamics of matter in the early universe, to properties of the exotic phases of quantum chromodynamics (QCD) produced at the LHC and the Relativistic Heavy Ion Collider (for overviews and reviews, see Refs. [7–15]). One of the major challenges facing quantum simulations of physical systems is the preparation of initial states on quantum computers that can be used to determine important quantities that are inaccessible to classical high-performance

computing, i.e., the problem of state preparation. While simulating the dynamics of any given initial state is known to be efficient for an ideal quantum computer [16], residing in the bounded-error quantum polynomial time complexity class, preparing an arbitrary state generally requires quantum resources that asymptotically scale superpolynomially with increasing system size [17], residing in the quantum Merlin-Arthur complexity class [18]. However, states of physical systems are not the general case, and are often constrained by both local and global symmetries [19]. In some instances, these symmetries allow observables to be computed by perturbing around states that can be efficiently initialized [9]. In the foreseeable future, quantum simulations will be far from asymptotic in both system size and evolution time, and the resources required for both time evolution and state preparation will be estimated by direct construction and extrapolations thereof. Furthermore, successful quantum simulations will require specialized quantum circuits and workflows that are optimized for specific quantum hardware.

The development of algorithms for preparing nontrivial initial states on quantum computers, including the ground states of quantum field theories (QFTs), is an active area of research. Even with many advances, the

*Corresponding authors: rolanf2@uw.edu

†marcilla@uw.edu

‡aciavare@uw.edu

§mjs5@uw.edu

Published by the American Physical Society under the terms of the [Creative Commons Attribution 4.0 International](https://creativecommons.org/licenses/by/4.0/) license. Further distribution of this work must maintain attribution to the author(s) and the published article’s title, journal citation, and DOI.

algorithms remain limited in capability, and generally do not scale favorably to modest-scale or large-scale simulations of quantum many-body systems. Consequently, quantum simulations of small model systems are currently being performed across an array of science domains, generally studying dynamics starting from tensor product initial states. While being the simplest gauge theory based on a continuous group, the Schwinger model [23] (quantum electrodynamics in $1 + 1$ dimensions) possesses many features of interest to the QCD and quantum information science communities. These include the presence of a mass gap, charge screening, a chiral condensate, few-body bound states (“hadrons” and “nuclei”), and a topological θ term. It has emerged as a popular test bed for developing quantum simulation techniques for lattice gauge theories, and has been explored with use of a variety of platforms, including trapped ions [24–27], superconducting qubits [28–34], photonic systems [35], Rydberg atoms [36], ultracold atoms [37–41], and classical electric circuits [42], together with classical simulations [22,43–61], calculations [62–69], and tensor networks [70–92] (for reviews on this last topic, see, e.g., Refs. [7,93]). There has also been pioneering work on quantum simulations of low-dimensional non-Abelian gauge theories, both with [94–99] and without [100–106] matter. While these are important benchmarks, more sophisticated simulations requiring the preparation of eigenstates or scattering states have so far been too demanding for noisy intermediate-scale quantum (NISQ) era quantum computers, and until now have been limited to 20 qubits [25,32].

Many systems of physical interest, including QCD, have translational symmetry and possess an energy (mass) gap Λ between the unique ground state and first excited state. The gap defines a characteristic length scale of the system $\xi = 1/\Lambda$, and parameterizes the decay of the longest distance correlations in the ground-state wave function,

falling as approximately $e^{-r/\xi}/r^\alpha$ for regions separated by $r \gg \xi$, for some α . A natural way to encode a lattice QFT onto a register of a digital quantum computer is by identifying subsets of qubits (or qudits) with spatial points of the lattice that align with the connectivity of the quantum computer. A realization of the ground state on the register of a quantum computer should reflect the localized correlations between these subsets of qubits separated by $r \gg \xi$ [107,108]. In the absence of topological order, one way to establish the ground state is to initialize the quantum register in a state without correlations between qubits, e.g., a tensor product state, and then systematically introduce correlations through the action of quantum circuits. A crucial point is that the localized correlations imply that the state preparation circuits need to have structure only for qubits spatially separated by $r \lesssim \xi$ [107,108]. This is sufficient to obtain exponentially converged accuracy in the prepared state. Because of translational invariance, the ground state for an arbitrarily large lattice can be prepared by repetition of these circuits across the entire register.

To study the dynamics of physically relevant systems in a quantitative way, with a complete quantification of uncertainties, simulations of large volumes of space-time are typically required. Motivated by the discussion in the previous paragraph, we introduce scalable circuits ADAPT-VQE (SC-ADAPT-VQE), a new method for quantum state preparation that uses the hierarchies of length scales present in physical systems; see Fig. 1 for an illustration. In SC-ADAPT-VQE, quantum circuits that (efficiently) prepare a given state to a specified level of precision are determined on modest-sized lattices that are large enough to contain the longest correlation lengths. As long as ξ is not too large, these circuits can be determined with the use of *classical* computers. This avoids the challenging task of optimizing circuits on a quantum computer with both statistical uncertainty and device noise [109,110]. Once

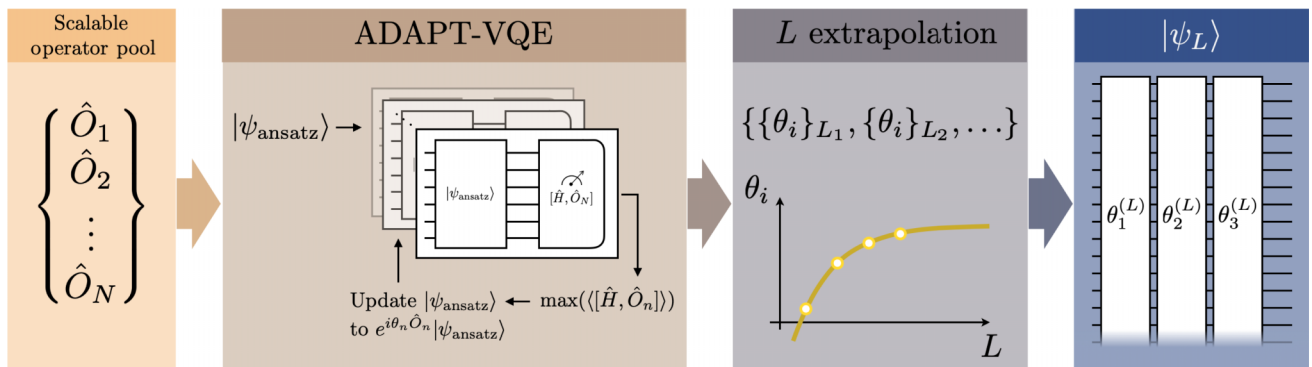


FIG. 1. Pictorial description of the SC-ADAPT-VQE algorithm. Once a pool of scalable operators $\{\hat{O}_i\}$ has been identified, ADAPT-VQE is performed with use of *classical* computers to determine a quantum circuit (parameterized by $\{\theta_i\}$) that prepares the vacuum up to a desired tolerance. ADAPT-VQE is repeated for multiple lattice sizes, $\{L_1, L_2, \dots\}$, and the circuit parameters are extrapolated to the desired L , which can be arbitrarily large. The extrapolated circuits are executed on a quantum computer to prepare the vacuum on a system of size L .

determined, (discrete) translation invariance is used to scale these circuits up to the full lattice. Since the quality of the prepared state becomes independent of the spatial lattice length L , with $\mathcal{O}(e^{-\xi/L})$ corrections, this is a potential path toward quantum simulations of lattice QFTs that are beyond the capabilities of high-performance computing.

In this work, SC-ADAPT-VQE is applied to the Schwinger model and is used to prepare the vacuum on up to 100 qubits on IBM's Eagle quantum processors. Underlying the development is the algorithm ADAPT-VQE [111] for quantum state preparation, which is modified to generate scalable circuits. After the necessary Trotterized circuits have been built, SC-ADAPT-VQE is performed with use of the Qiskit classical simulator on system sizes up to $L = 14$ (28 qubits). It is found that both the energy density and the chiral condensate converge exponentially with circuit depth to the exact results. Importantly, both the quality of the prepared state and the structure of the associated circuits are found to converge with system size. This allows the state preparation circuits, determined on small lattices with use of classical computing, to be extrapolated to much larger lattices, with a quality that becomes independent of L . The scaled circuits are used to prepare the $L \leq 500$ vacua with use of Qiskit's matrix product state (MPS) circuit simulator, and to prepare the $L \leq 50$ (100 qubits) vacua on the registers of IBM's superconducting-qubit quantum computers `ibm_brisbane` and `ibm_cusco`. An improved and unbiased error-mitigation technique, operator decoherence renormalization (ODR), is developed and applied to the quantum simulations to estimate error-free observables. The results obtained from both the MPS circuit simulator and IBM's quantum computers are found to be in excellent agreement with density matrix renormalization group (DMRG) calculations.

II. THE LATTICE SCHWINGER MODEL

The Schwinger model [23] has a long history of study in the continuum and with use of numerical lattice techniques. In the continuum, it is described by the Lagrange density

$$\mathcal{L} = \bar{\psi} (i\not{D} - m_\psi) \psi - \frac{1}{4} F^{\mu\nu} F_{\mu\nu}. \quad (1)$$

Electrically charged fermions are described by the field operator ψ with mass m_ψ , the electromagnetic gauge field is described by A_μ with field tensor $F_{\mu\nu}$, and the covariant derivative is defined as $D_\mu = \partial_\mu - ieA_\mu$. It is the Hamiltonian lattice formulation, first developed and studied by Banks, Kogut, and Susskind [112,113], that is relevant for quantum simulations. One feature of gauge theories in $1 + 1$ dimensions, which distinguishes them from theories in higher dimensions, is that the gauge field is completely constrained by the distribution of fermion charges through Gauss's law. In axial gauge, the spatial gauge

field is absent, and the effects of the time component of the gauge field are included by nonlocal (Coulomb) interactions [83,97]. With open boundary conditions (OBCs), use of the staggered fermion discretization [112] of the electron field, and application of the Jordan-Wigner transformation to map fermion field operators to spins, the Schwinger model Hamiltonian is (for a derivation, see, e.g., Ref. [25])

$$\begin{aligned} \hat{H} &= \hat{H}_m + \hat{H}_{\text{kin}} + \hat{H}_{\text{el}} = \frac{m}{2} \sum_{j=0}^{2L-1} \left[(-1)^j \hat{Z}_j + \hat{I} \right] \\ &+ \frac{1}{2} \sum_{j=0}^{2L-2} \left(\hat{\sigma}_j^+ \hat{\sigma}_{j+1}^- + \text{H.c.} \right) + \frac{g^2}{2} \sum_{j=0}^{2L-2} \left(\sum_{k \leq j} \hat{Q}_k \right)^2, \\ \hat{Q}_k &= -\frac{1}{2} \left[\hat{Z}_k + (-1)^k \hat{I} \right], \end{aligned} \quad (2)$$

where L is the number of spatial lattice sites, corresponding to $2L$ staggered (fermion) sites, m and g are the (bare) electron mass and charge, respectively, and the staggered lattice spacing a has been set to 1 [115]. "Physical" quantities are derived from the corresponding dimensionless quantities by restoring factors of the spatial lattice spacing. Even (odd) sites correspond to electrons (positrons), as reflected in the staggered mass term and charge operator [116]. A background electric field can be included straightforwardly, equivalent to a θ term, but will be set to zero in this work. In the sector with vanishing total electric charge, \hat{H}_{el} in Eq. (2) can be rewritten in a way that reduces the number of gates required in quantum circuits for time evolution, and is less demanding on device connectivity; see Appendix A. Because of confinement, the low-energy excitations are hadrons and the mass gap is given by $\Lambda = m_{\text{hadron}}$. For our purposes, m_{hadron} is defined to be the energy difference in the $Q = 0$ sector between the first excited state (single hadron at rest) and the vacuum.

A. Infinite-volume extrapolations of local observables

Central to the development of state preparation circuits is the scaling of expectation values of local observables in the ground state, with both the correlation length $\xi = 1/m_{\text{hadron}}$ and the volume L . Because of the exponential suppression of correlations in the ground state between regions separated by $r > \xi$, it is expected that, locally, the wave function has converged to its infinite-volume form, with corrections of $\mathcal{O}(e^{-\xi/L})$. As a result, expectation values of local observables will be exponentially converged to their infinite-volume values. However, near the boundaries of the lattice, the wave function is perturbed over a depth proportional to ξ , causing local observables to deviate from their infinite-volume values. Equivalently, boundary effects cause deviations in volume averages of local

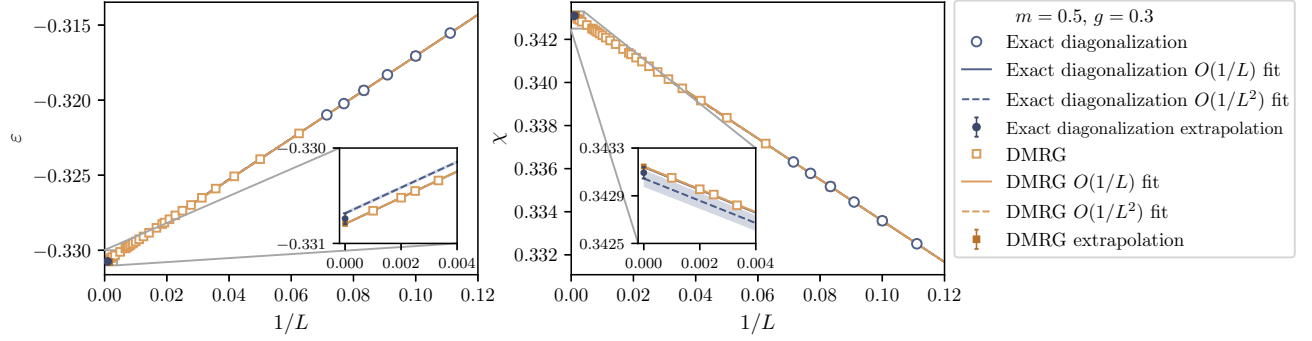


FIG. 2. L extrapolations of the vacuum energy density ε (left) and the chiral condensate χ (right) for $m = 0.5$ and $g = 0.3$. The results of exact diagonalization calculations for $L \geq 9$ (blue circles) given in Table I and DMRG calculations (orange squares) given in Table V are extrapolated to $L \rightarrow \infty$, as shown by the darker points. The solid lines correspond to linear extrapolations and the dashed lines correspond to quadratic extrapolations, and are found to overlap (see the insets). The difference between the $L \rightarrow \infty$ values of these two extrapolations defines the (fitting) uncertainties associated with the darker points.

observables that are $\mathcal{O}(\xi/L)$. This scaling of observables is responsible for the SC-ADAPT-VQE prepared vacuum converging exponentially in circuit depth, and enables the circuits to be systematically extrapolated to larger system sizes.

Two quantities associated with the ground-state wave function (vacuum) that we focus on are the chiral condensate χ and the energy density ε . The chiral condensate [117] is an order parameter of chiral symmetry breaking, and in the Jordan-Wigner mapping is given by

$$\chi = \frac{1}{2L} \sum_{j=0}^{2L-1} \langle (-1)^j \hat{Z}_j + \hat{I} \rangle \equiv \frac{1}{2L} \sum_{j=0}^{2L-1} \chi_j. \quad (3)$$

The energy density is defined as $\varepsilon = \langle \hat{H} \rangle / L$, and in axial gauge is not a local observable because the contribution from the electric field term in the Hamiltonian, \hat{H}_{el} , involves all-to-all couplings. However, this is an artifact of using axial gauge and enforcing Gauss's law. In Weyl gauge, with explicit (local) gauge degrees of freedom, the

Hamiltonian is manifestly local, and therefore the energy density is a local observable. These quantities are computed for $m = 0.5$ and $g = 0.3$ with use of exact diagonalization for $L \leq 14$ (Table I) and DMRG calculations for $L \gg 14$ (Table V). As anticipated, a linear extrapolation in $1/L$ is found to be consistent with these results, as seen in Fig. 2. Additional details, along with results for $m = 0.1$ with $g = 0.3$ and $g = 0.8$, can be found in Appendix B.

III. SC-ADAPT-VQE FOR THE LATTICE SCHWINGER MODEL

Underlying SC-ADAPT-VQE is ADAPT-VQE [111], a quantum algorithm for state preparation that has been applied to spin models [118], systems in quantum chemistry [111, 119–124], and nuclear structure [125, 126]. It builds upon the variational quantum eigensolver (VQE) [127], in which parameterized quantum circuits are optimized to minimize the expectation value of a Hamiltonian. The parameterized circuits are constructed stepwise (or equivalently in layers), where the incrementally improved

TABLE I. Energy density, chiral condensate, and wave function infidelity for the vacuum of the Schwinger model with $m = 0.5$ and $g = 0.3$. Both the results obtained from seven steps of the SC-ADAPT-VQE (aVQE) algorithm with use of Qiskit's classical simulator and the exact values are given. The last column shows the number of CNOT gates per qubit in the state preparation circuit.

L	$\varepsilon^{(\text{aVQE})}$	$\varepsilon^{(\text{exact})}$	$\chi^{(\text{aVQE})}$	$\chi^{(\text{exact})}$	\mathcal{I}_L	CNOT gates per qubit
6	-0.30772	-0.30791	0.32626	0.32720	0.00010	31.2
7	-0.31097	-0.31117	0.32847	0.32947	0.00011	33.6
8	-0.31348	-0.31363	0.33036	0.33118	0.00008	35.8
9	-0.31539	-0.31553	0.33171	0.33251	0.00008	37.1
10	-0.31691	-0.31706	0.33279	0.33358	0.00008	38.2
11	-0.31816	-0.31831	0.33367	0.33445	0.00008	39.1
12	-0.31920	-0.31935	0.33441	0.33517	0.00008	39.8
13	-0.32008	-0.32023	0.33504	0.33578	0.00008	40.5
14	-0.32084	-0.32098	0.33557	0.33631	0.00008	41.0

ansatz states converge to the ground state with successive iterations. At each step, the unitary transformation that maximally decreases the energy of the ansatz state is identified from a predefined set (“pool”) of unitaries. The quantum circuit corresponding to this unitary is then appended to the state preparation circuit. The (initial) state from which the algorithm starts will often be chosen to be a tensor product or an entangled state that can be efficiently prepared on a quantum computer, such as a Greenberger-Horne-Zeilinger state. If the target state is the ground state of a confining gauge theory, e.g., the Schwinger model, the strong-coupling (trivial) vacuum,

$$|\Omega_0\rangle = |\uparrow\downarrow\uparrow\downarrow \dots \uparrow\downarrow\rangle, \quad (4)$$

can be a good choice for such an initial state as it has the correct long-distance structure in the gauge fields. The ADAPT-VQE algorithm can be summarized as follows:

- (1) Define a pool of operators $\{\hat{O}\}$ that are constrained to respect some or all of the symmetries of the system.
- (2) Initialize the register of the quantum computer to a strategically selected state, $|\psi_{\text{ansatz}}\rangle$, with the desired quantum numbers and symmetries of the target wave function.
- (3) Measure the expectation value of the commutator of the Hamiltonian with each operator in the pool, $\langle\psi_{\text{ansatz}}|[\hat{H}, \hat{O}_i]|\psi_{\text{ansatz}}\rangle$. These are estimators of the associated decrease in energy from transforming the ansatz wave function by $|\psi_{\text{ansatz}}\rangle \rightarrow e^{i\theta_i\hat{O}_i}|\psi_{\text{ansatz}}\rangle$, for an arbitrary parameter θ_i .
- (4) Identify the operator, \hat{O}_n , with the largest magnitude commutator with the Hamiltonian. If the absolute value of this commutator is below some predetermined threshold, terminate the algorithm. If it is above the threshold, update the ansatz with the parameterized evolution of the operator $|\psi_{\text{ansatz}}\rangle \rightarrow e^{i\theta_n\hat{O}_n}|\psi_{\text{ansatz}}\rangle$.
- (5) Use VQE to find the values of the variational parameters that minimize the energy, $\langle\psi_{\text{ansatz}}(\theta_1, \theta_2, \dots, \theta_n)|\hat{H}|\psi_{\text{ansatz}}(\theta_1, \theta_2, \dots, \theta_n)\rangle$. The previously optimized values for $\theta_{1,2,\dots,n-1}$ and $\theta_n = 0$, are used as initial conditions. If the optimal value of the newest parameter, θ_n , is below some predetermined threshold, terminate the algorithm.
- (6) Return to step 3.

For a given pool of operators, it is *a priori* unknown if this algorithm will furnish a wave function that satisfies the predetermined threshold for the observable(s) of interest, but it is expected that the pool can be expanded on the fly to achieve the desired threshold. The systems that have been explored with this algorithm show, for a fixed pool, exponential convergence with increasing numbers of iterations [111,119,122,124,125].

Generally, different terms contributing to operators in the pool do not commute with each other. Constructing quantum circuits that exactly implement the exponential of a sum of noncommuting terms is challenging, and in practice approximations such as first-order Trotterization are used. This introduces (higher-order) systematic deviations from the target unitary operator in each case, and defines the pool of unitary operators,

$$\{\hat{U}_i\} = \{\exp(i\theta_i\hat{O}_i)\} \rightarrow \left\{ \prod_t \hat{U}_i^{(t)} \right\}. \quad (5)$$

These Trotterized unitary operators correspond to the quantum circuits that are implemented in state preparation. In optimization of the quality of the state prepared on a given quantum computer, particularly a NISQ era device, there are trade-offs between the gate depth of a particular circuit implementation, the coherence time, the errors associated with gate operations, and the associated Trotter errors. This is explored in Appendix C.

Typically, ADAPT-VQE is a hybrid classical-quantum algorithm that evaluates matrix elements of the Hamiltonian in trial wave functions on a quantum computer, with parameters that are optimized classically. One disadvantage of this is that the evaluation of expectation values of the Hamiltonian requires a large number of measurements (shots) on quantum computers. A novel part of SC-ADAPT-VQE is the use of a *classical* simulator to determine the ADAPT-VQE state preparation circuits. As shown in Sec. V, these circuits can be scaled and used to prepare the vacuum on arbitrarily large lattices.

A. A scalable operator pool for the lattice Schwinger model

A successful application of SC-ADAPT-VQE to the preparation of the lattice Schwinger model vacuum requires choosing an efficient and scalable pool of operators (first step in Fig. 1). These operators are used to systematically improve the ansatz vacuum wave function, and are (only) constrained to be charge neutral, symmetric under charge conjugation and parity (*CP*), and, as a consequence of the *CPT* theorem [128–130], invariant under time reversal [131]. Ideally one wants to find the smallest pool of operators that is expressive enough to converge rapidly toward the vacuum. For a lattice with OBCs, the system has translational symmetry in the volume that is broken by the boundaries (surface). In the vacuum, the effects of the boundaries are expected to be localized, with penetration depths set by the mass gap. Therefore, the pool of operators should contain translationally invariant “volume” operators, and “surface” operators that have support only near the boundaries. In addition, a hierarchy is anticipated in which one-body operators are more important than two-body operators, two-body operators

are more important than three-body operators, and so on [132]. Note that because wave functions are evolved with $\exp(i\theta_i \hat{O}_i)$, arbitrarily high-body correlations are built from n -body operators (analogous to connected versus disconnected Feynman diagrams). For the Schwinger model, we observe that one-body operators are sufficient.

With the above discussion as guidance, it is convenient to define two classes of one-body operators, one containing volume operators and the other containing surface operators:

$$\begin{aligned}\hat{O}_m^V &= \frac{1}{2} \sum_{n=0}^{2L-1} (-1)^n \hat{Z}_n, \\ \hat{O}_h^V(d) &= \frac{1}{4} \sum_{n=0}^{2L-1-d} \left(\hat{X}_n \hat{Z}^{d-1} \hat{X}_{n+d} + \hat{Y}_n \hat{Z}^{d-1} \hat{Y}_{n+d} \right), \\ \hat{O}_m^S(d) &= (-1)^d \frac{1}{2} \left(\hat{Z}_d - \hat{Z}_{2L-1-d} \right), \\ \hat{O}_h^S(d) &= \frac{1}{4} \left(\hat{X}_1 \hat{Z}^{d-1} \hat{X}_{d+1} + \hat{Y}_1 \hat{Z}^{d-1} \hat{Y}_{d+1} \right. \\ &\quad \left. + \hat{X}_{2L-2-d} \hat{Z}^{d-1} \hat{X}_{2L-2} + \hat{Y}_{2L-2-d} \hat{Z}^{d-1} \hat{Y}_{2L-2} \right).\end{aligned}\quad (7)$$

Unlabeled \hat{Z} 's act on the qubits between the leftmost and rightmost operators (e.g., $\hat{X}_0 \hat{Z}^2 \hat{X}_3 = \hat{X}_0 \hat{Z}_1 \hat{Z}_2 \hat{X}_3$). The first two operators in Eq. (7) are translationally invariant, \hat{O}_m^V is the mass term in the Hamiltonian, and $\hat{O}_h^V(d)$ is a generalized hopping term that spans an odd number of fermion sites, d , connecting electrons and positrons at spatial sites separated by $\Delta L = (d-1)/2$. Only d -odd operators are retained, as the d -even operators break CP symmetry. The second two operators in Eq. (7) correspond to surface terms, of the form of a mass density and of a hopping density at and near the boundaries. For $\hat{O}_h^V(d)$, $d \in \{1, 3, \dots, 2L-3\}$, and for $\hat{O}_h^S(d)$, $d \in \{1, 3, \dots, 2L-5\}$, preventing hopping between boundaries (which is found to improve convergence).

Time-reversal symmetry implies that the vacuum wave function can be made real up to an overall phase. The SC-ADAPT-VQE ansatz is built from unitaries of the form $e^{i\theta_i \hat{O}_i}$, and furnishing a real wave function requires that the operators in the pool are imaginary and antisymmetric. The operators in Eq. (7) are real and are therefore disqualified from being members of the pool. Instead, consider a pool comprised of their commutators [133]:

$$\{\hat{O}\} = \left\{ \hat{O}_{mh}^V(d), \hat{O}_{mh}^S(0, d), \hat{O}_{mh}^S(1, d) \right\},$$

$$\begin{aligned}\hat{O}_{mh}^V(d) &\equiv i \left[\hat{O}_m^V, \hat{O}_h^V(d) \right] \\ &= \frac{1}{2} \sum_{n=0}^{2L-1-d} (-1)^n \left(\hat{X}_n \hat{Z}^{d-1} \hat{Y}_{n+d} - \hat{Y}_n \hat{Z}^{d-1} \hat{X}_{n+d} \right), \\ \hat{O}_{mh}^S(0, d) &\equiv i \left[\hat{O}_m^S(0), \hat{O}_h^V(d) \right] = \frac{1}{4} \left(\hat{X}_0 \hat{Z}^{d-1} \hat{Y}_d - \hat{Y}_0 \hat{Z}^{d-1} \hat{X}_d \right. \\ &\quad \left. - \hat{Y}_{2L-1-d} \hat{Z}^{d-1} \hat{X}_{2L-1} + \hat{X}_{2L-1-d} \hat{Z}^{d-1} \hat{Y}_{2L-1} \right), \\ \hat{O}_{mh}^S(1, d) &\equiv i \left[\hat{O}_m^S(1), \hat{O}_h^S(d) \right] = \frac{1}{4} \left(\hat{Y}_1 \hat{Z}^{d-1} \hat{X}_{d+1} \right. \\ &\quad \left. - \hat{X}_1 \hat{Z}^{d-1} \hat{Y}_{d+1} + \hat{Y}_{2L-2-d} \hat{Z}^{d-1} \hat{X}_{2L-2} \right. \\ &\quad \left. - \hat{X}_{2L-2-d} \hat{Z}^{d-1} \hat{Y}_{2L-2} \right).\end{aligned}\quad (8)$$

While the contributions to extensive quantities from the volume operators, \hat{O}^V , typically scale as $\mathcal{O}(L)$, the surface operators, \hat{O}^S , make $\mathcal{O}(1)$ contributions as they are constrained to regions near the boundaries [134]. When acting on the strong-coupling vacuum, the exponential of an operator in the pool creates and annihilates e^+e^- pairs separated by distance d . As the operators that are being considered are one-body operators, the variational algorithm is essentially building a coupled-cluster singles state (see, e.g., Refs. [135,136]).

IV. SCALABLE QUANTUM CIRCUITS FROM CLASSICAL COMPUTING

Integral to the application of SC-ADAPT-VQE is performing ADAPT-VQE on a series of systems that are large enough to enable a robust scaling of the parameterized circuits. These scalable circuits can be determined either with classical computing or by use of a smaller partition of a larger quantum computer. In this section, application of SC-ADAPT-VQE implemented with use of the Qiskit noiseless classical simulator [137,138] is reported.

A. Trotterized quantum circuits for the scalable operator pool

As discussed above, implementation of the unitary operators in the pool, i.e., Eq. (5), on classical simulators or quantum computers requires their mapping to sequences of quantum gates. For the individual terms in Eq. (8), we have chosen to do this using Trotterization. The optimal gate decomposition is less important for implementation using a classical simulator, but is crucial for successful simulations on a quantum computer. With the goal of using IBM's superconducting-qubit quantum computers [137,138], our circuit designs aim to minimize two qubit gate count and circuit depth and require only nearest-neighbor connectivity.

As can be seen in Eq. (8), each term in a given operator in the pool is of the form $(\hat{X} \hat{Z}^{d-1} \hat{Y} - \hat{Y} \hat{Z}^{d-1} \hat{X})$ for

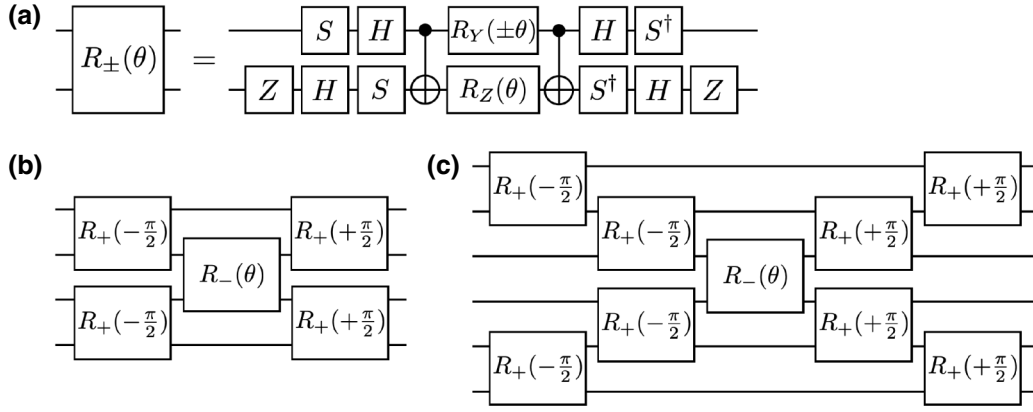


FIG. 3. (a) Definition of the $R_{\pm}(\theta)$ gate, which implements $\exp[-i\theta/2(\hat{Y}\hat{X} \pm \hat{X}\hat{Y})]$. The $R_{\pm}(\theta)$ gate is used to implement (b) $\exp[-i\theta/2(\hat{X}\hat{Z}^2\hat{Y} - \hat{Y}\hat{Z}^2\hat{X})]$ and (c) $\exp[i\theta/2(\hat{X}\hat{Z}^4\hat{Y} - \hat{Y}\hat{Z}^4\hat{X})]$ (note the change in sign).

some odd value of d . The construction of circuits implementing the corresponding unitary operators follows the strategy outlined in Ref. [139]. First, consider the Trotterization of terms with $d = 1$, i.e., constructing a circuit corresponding to $e^{i\theta/2(\hat{X}\hat{Y} \pm \hat{Y}\hat{X})} \equiv R_{\pm}(\theta)$. There is a known two-controlled-NOT (CNOT) realization of this unitary operator [139], shown in Fig. 3(a). For terms with $d > 1$, this circuit can be extended in an X pattern as shown in Figs. 3(b) and 3(c) for $d = 3$ and $d = 5$, respectively [140]. Terms with larger d are constructed by extension of the legs of the X. Compared with the traditional CNOT-staircase-based circuits, there is a reduction by two CNOT gates, and a reduction by a factor of 2 in CNOT depth [141].

However, the primary advantage of these circuits is that they allow an efficient arrangement of terms leading to cancellations among neighboring $R_+(\pm\pi/2)$ gates. As depicted in Fig. 4, this is made possible by arranging the circuit elements so that sequential terms are offset by $d - 1$ qubits, i.e., start on qubit $\{0, d - 1, 2(d - 1), \dots\}$. This allows the

outermost gates to cancel (using the identity in the upper left of Fig. 4). Also, for $d \geq 5$, the next layer should start $(d - 1)/2$ qubits below the previous one, as the circuit depth can be reduced by interleaving the legs of the X. Further optimizations are possible by our noting that distinct orderings of terms, while equivalent up to higher-order Trotter errors, can have different convergence properties; see Appendix C.

B. Building scalable state preparation quantum circuits using SC-ADAPT-VQE with classical computing

In this section, SC-ADAPT-VQE is used to prepare approximations to the vacuum of the lattice Schwinger model on up to $L = 14$ spatial sites (28 qubits) using classical simulations of the quantum circuits developed in the previous section (second step in Fig. 1).

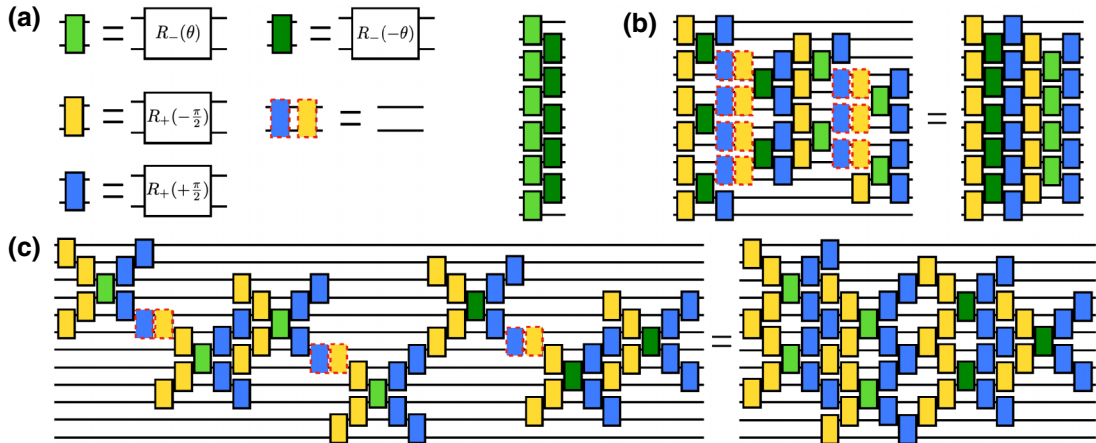


FIG. 4. Simplifications of quantum circuits for the Trotterized unitaries corresponding to (a) $\hat{O}_{mh}^V(1)$, (b) $\hat{O}_{mh}^V(3)$, and (c) $\hat{O}_{mh}^V(5)$ for $L = 6$, as explained in the main text. Cancellations between $R_+(\pm\pi/2)$ are highlighted with red-dash-outlined boxes.

In addition to the energy density and chiral condensate introduced in Sec. II A, the infidelity density,

$$\mathcal{I}_L = \frac{1}{L} (1 - |\langle \psi_{\text{ansatz}} | \psi_{\text{exact}} \rangle|^2), \quad (9)$$

is also studied, where $|\psi_{\text{exact}}\rangle$ is the exact vacuum wave function on a lattice with L spatial sites. An infidelity density that is constant in L corresponds to constant deviations in local observables evaluated in the prepared state.

To investigate the interplay between L and $\xi = 1/m_{\text{hadron}}$, three sets of parameters are considered: $m = 0.1$ and $g = 0.3$ ($\xi_{L=14} = 2.6$), $m = 0.1$ and $g = 0.8$ ($\xi_{L=14} = 1.3$), and $m = 0.5$ and $g = 0.3$ ($\xi_{L=14} = 0.9$). The ξ are determined with exact diagonalization, and are found to weakly depend on L . Note that increasing either m or g decreases the correlation length. To make systematically

improvable predictions of observables from the QFT that emerges from a given lattice model, extrapolations to the continuum (lattice spacing to zero) and infinite-volume ($L \rightarrow \infty$) limits must be performed. This requires that the relevant correlation length or lengths are all much greater than the lattice spacing, $\xi \gg 1$ in lattice units, but are well contained in the lattice volume, $L \gg \xi$. We primarily focus on extrapolation to large lattices, and therefore require only $L \gg \xi$. As a result, the parameter set $m = 0.5$ and $g = 0.3$ is used as the primary example throughout this work.

The values of ε , χ , and \mathcal{I}_L obtained at the seventh step of SC-ADAPT-VQE with $m = 0.5$ and $g = 0.3$ are given in Table I, while their deviations from the exact values are shown in Fig. 5, as a function of increasing number of SC-ADAPT-VQE steps. The corresponding numerical values obtained from the other parameter sets are presented in Appendix F [142]. As seen by their approximately linear

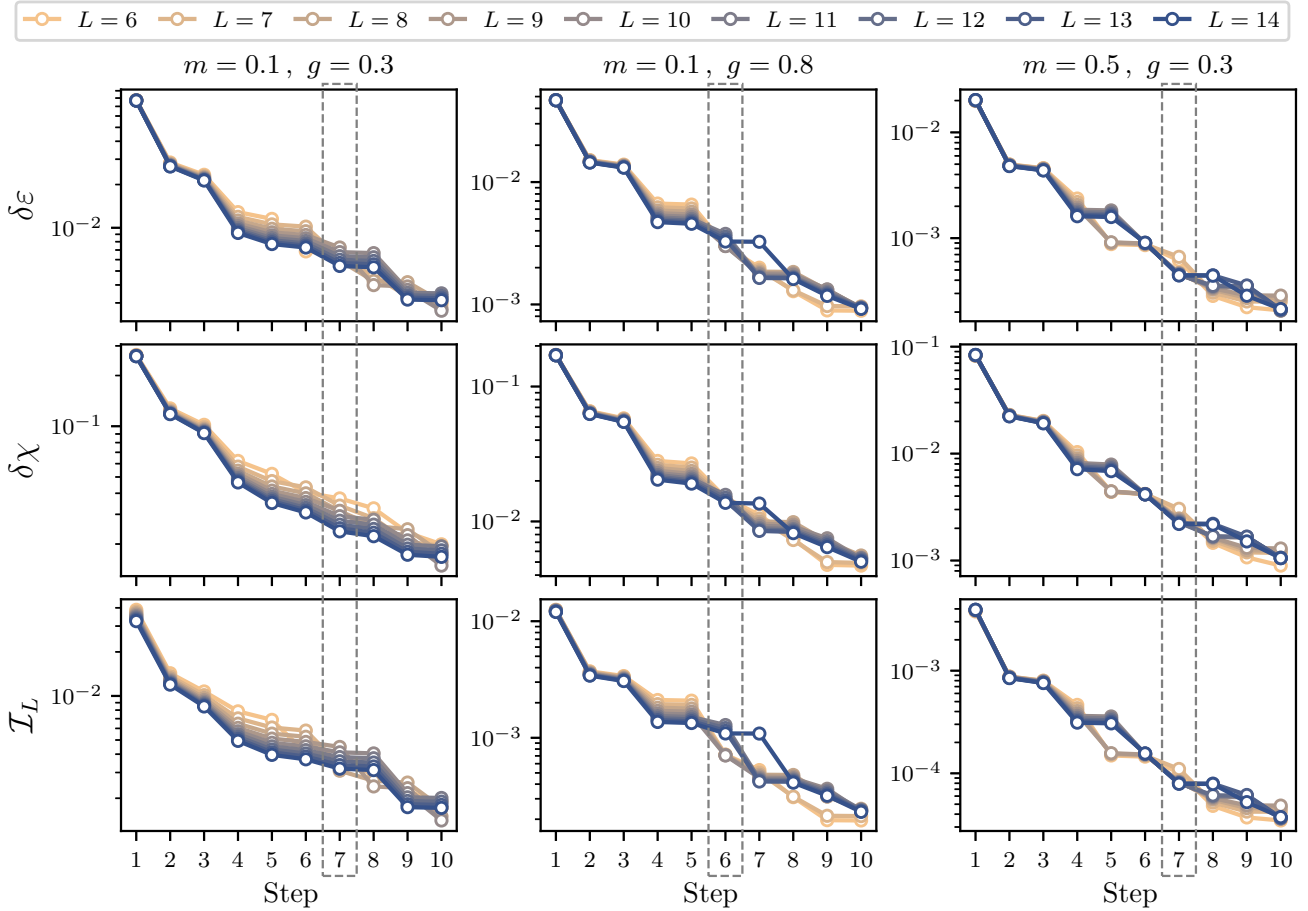


FIG. 5. Deviations from the exact values of the energy density $\delta\varepsilon$, chiral condensate $\delta\chi$, and wave function infidelity density \mathcal{I}_L obtained with SC-ADAPT-VQE. The deviation in quantity “ x ” is defined as $\delta x = |(x^{(\text{aVQE})} - x^{(\text{exact})})/x^{(\text{exact})}|$, where $x^{(\text{exact})}$ denotes the exactly calculated value at the same L . Results are shown for $L = 6$ to $L = 14$ as a function of step number for $m = 0.1$ and $g = 0.3$ (left column), $m = 0.1$ and $g = 0.8$ (center column), and $m = 0.5$ and $g = 0.3$ (right column). The numerical values for $m = 0.5$ and $g = 0.3$ for the seventh step (highlighted with the dashed box) are given in Table I, and the sequencing of the corresponding Trotterized operators and the variational parameters are given in Table II. The corresponding results for $m = 0.1$ and $g = 0.3$ (seventh step) and for $m = 0.1$ and $g = 0.8$ (sixth step) can be found in Appendix F.

TABLE II. Structure of the ansatz wave function with $m = 0.5$ and $g = 0.3$ through seven steps of the SC-ADAPT-VQE algorithm obtained from a classical simulation using Qiskit. For a given L , the order that the operators are added to the ansatz is displayed from left to right, with the associated parameter, θ_i , given as the entry in the table. The operators, $\hat{O}_{mh}^V(d_h)$ and $\hat{O}_{mh}^S(d_m, d_h)$, are defined in Eq. (8). An entry of “–” means that the operator does not contribute. The bottom row corresponds to an extrapolation to $L = \infty$ as detailed in Eq. (10).

L	θ_i								
	$\hat{O}_{mh}^V(1)$	$\hat{O}_{mh}^V(3)$	$\hat{O}_{mh}^V(5)$	$\hat{O}_{mh}^V(1)$	$\hat{O}_{mh}^V(7)$	$\hat{O}_{mh}^S(0, 1)$	$\hat{O}_{mh}^V(7)$	$\hat{O}_{mh}^V(1)$	$\hat{O}_{mh}^S(0, 3)$
6	0.18426	-0.03540	0.00731	0.11866	–	0.06895	-0.00182	–	-0.03145
7	0.18440	-0.03574	0.00729	0.11864	–	0.06867	-0.00177	–	-0.03066
8	0.13931	-0.03727	0.00760	0.08870	–	0.06925	-0.00183	0.07457	–
9	0.13945	-0.03714	0.00755	0.08849	–	0.06904	-0.00180	0.07473	–
10	0.13956	-0.03703	0.00752	0.08832	-0.00178	0.06888	–	0.07485	–
11	0.13965	-0.03695	0.00749	0.08819	-0.00177	0.06875	–	0.07494	–
12	0.13972	-0.03688	0.00747	0.08808	-0.00176	0.06865	–	0.07502	–
13	0.13977	-0.03683	0.00745	0.08800	-0.00175	0.06856	–	0.07508	–
14	0.13982	-0.03678	0.00744	0.08793	-0.00174	0.06849	–	0.07513	–
∞	0.1400	-0.0366	0.0074	0.0877	-0.0017	0.0682	–	0.0753	–

behavior in the log plots in Fig. 5, the error in each of these quantities decreases exponentially with algorithm step, indicating convergence to the target wave function. This exponential trend is demonstrated out to ten steps, reaching a convergence comparable to the systematic errors introduced in the L extrapolations below. This provides evidence that this choice of initial state and operator pool does not suffer from “barren plateaus” or local minima. For a given step in the algorithm, the error is seen to become independent of system size. This indicates that extrapolations of the circuits to arbitrarily large systems will have errors that are *independent of L* . As discussed above, it is expected that SC-ADAPT-VQE will converge more rapidly for systems with smaller correlation lengths. This is indeed seen in Fig. 5, where the correlation length decreases from left to right, while the convergence improves. Also included in Table I is the number of CNOT gates per qubit in the SC-ADAPT-VQE circuit. It is seen to scale as a constant plus a subleading $\mathcal{O}(1/L)$ term, leading to an asymptotic value of 48 CNOT gates per qubit. This scaling is due to there being $(2L - d)$ terms in each volume operator.

The structure of the SC-ADAPT-VQE state preparation circuit and the corresponding variational parameters for $m = 0.5$ and $g = 0.3$ are given in Table II. Notice that initially localized operators are added to the wave function (small d), followed by increasingly longer-range ones, as well as surface operators. Systems with longer correlation lengths require larger d operators (e.g., compare Tables II and VI), in line with previous discussions on the exponential decay of correlations for $d > \xi$. It is also seen that the surface operators become less important (appear later in the ansatz structure) for larger lattices. For example, as shown in Table II, the fifth step of SC-ADAPT-VQE transitions from being a surface operator to a volume operator at $L = 10$ (causing the jump in convergence at the fifth

step in the right column in Fig. 5). This is expected as they contribute $\mathcal{O}(1/L)$ to the energy density, whereas volume operators contribute $\mathcal{O}(1)$.

Importantly, Table II shows that the order of operators and the corresponding variational parameters are converging with increasing system size (third step in Fig. 1). This is due to exponentially decaying correlations for $d \gg \xi$, and it is expected that the variational parameters will also converge exponentially, once L is sufficiently large to contain ξ , and we assume the following form:

$$\theta_i = \theta_i^{L=\infty} + c_1 e^{-c_2 L}. \quad (10)$$

Table II shows that this convergence sets in for $L > 7$ [143], and the variational parameters extrapolated to $L = \infty$ are given in the last row of Table II. These are used in the next section to initialize the vacuum on lattices up to $L = 500$. An example of extrapolating the variational parameters is shown in Fig. 6 for the parameter θ_1 , associated with $\hat{O}_{mh}^V(1)$. The exact results obtained for $L \leq 14$ are well reproduced and extrapolated with the exponential functional form in Eq. (10) [144]. A more comprehensive discussion of the parameter extrapolations, along with examples for $m = 0.1$ and $g = 0.3$ and for $m = 0.1$ and $g = 0.8$, can be found in Appendix D.

V. PREPARING THE VACUUM OF THE SCHWINGER MODEL ON LARGE LATTICES

The vacuum preparation circuits, determined for $L \leq 14$ with SC-ADAPT-VQE using an exact (state vector) classical simulator, are scaled to prepare the vacuum on much larger lattices. These scaled circuits are used to prepare the vacuum on lattices of up to $L = 500$ (1000 qubits) with use of a classical MPS circuit simulator and up to $L = 50$ (100 qubits) with use of IBM’s Eagle-processor

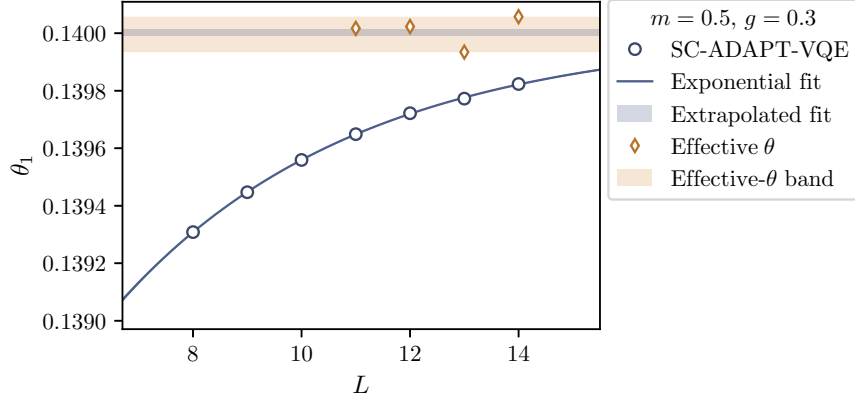


FIG. 6. Example of fitting the asymptotic L dependence of a parameter defining the SC-ADAPT-VQE state-preparation circuit. The results for θ_1 , corresponding to evolving by $\hat{O}_{mh}^V(1)$ (blue circles), determined from classical simulations, for $m = 0.5$ and $g = 0.3$ given in Table II, are extrapolated to $L = \infty$ by (i) use of a three-parameter fit given in Eq. (10), as shown by the blue line, with an asymptotic value shown by the blue region, and by (ii) the forming of effective θ (orange diamonds) defined in Eq. (D3), with the maximum and minimum values shown as the orange shaded region.

quantum computers (fourth step in Fig. 1). We emphasize that this scaling requires no further optimization of the circuits. The chiral condensate and energy density determined from the classical simulator are found to be consistent with DMRG calculations. On the quantum computers, the chiral condensate and charge-charge correlators are measured to probe the quality of one-qubit and two-qubit observables. The results are in agreement with those from the classical MPS simulator, within statistical uncertainties.

A. Classical simulation

Very large quantum circuits that do not generate long-range entanglement can be efficiently simulated with use of the Qiskit `matrix_product_state` classical simulator. Here it is used to simulate the preparation of the Schwinger model vacuum on $L \gg 14$ lattices, applying the scalable circuits determined in the previous section from seven steps of SC-ADAPT-VQE on $L \leq 14$ lattices. The values obtained for the chiral condensate and energy density up to $L = 500$ are compared with DMRG results, and are presented in Table III. The deviations in the energy density (approximately 1×10^{-4}) and chiral condensate (approximately 1×10^{-3}) are in good agreement with what was found for smaller L ; see Table I. This demonstrates that the systematic errors in the vacuum wave functions prepared with the scaled quantum circuits are (approximately) independent of L over this range of lattice volumes [145]. The scaled circuits corresponding to $m = 0.1$ and $g = 0.3$ and for $m = 0.1$ and $g = 0.8$ were also used to successfully prepare the vacuum. However, because of the longer correlation lengths, MPS calculations with $L \gtrsim 100$ required excessive classical resources, and were not performed. See Appendix F for more details.

It is worth summarizing what has been accomplished in this work with classical simulations:

- (1) In Sec. II, the vacuum energy density and chiral condensate were determined exactly for $L \leq 14$ (28 staggered lattice sites) with use of exact diagonalization and for $L \leq 10^3$ with use of DMRG calculations. The results for $L \geq 9$ were (consistently) extrapolated to $L \rightarrow \infty$, with $1/L$ scaling.
- (2) In Sec. IV, SC-ADAPT-VQE, based on the scalable operator pool determined in Sec. III, was performed on $L \leq 14$ lattices. Intensive quantities were found to converge exponentially with circuit depth, and the errors in these quantities, as well as the structure of the state preparation circuits, were found to become independent of L . This enabled the variational parameters defining the state preparation circuits to be consistently extrapolated to arbitrarily large L .

TABLE III. Results for large lattices with $m = 0.5$ and $g = 0.3$ through seven steps of SC-ADAPT-VQE using circuits scaled from $L \leq 14$. The superscript “SC-MPS” denotes the results obtained from the scaled circuits using the Qiskit MPS classical simulator, and the superscript “DMRG” denotes results obtained from DMRG calculations.

L	$\varepsilon^{(\text{SC-MPS})}$	$\varepsilon^{(\text{DMRG})}$	$\chi^{(\text{SC-MPS})}$	$\chi^{(\text{DMRG})}$
50	-0.32790	-0.32805	0.34044	0.34123
100	-0.32928	-0.32942	0.34135	0.34219
200	-0.32996	-0.33011	0.34181	0.34267
300	-0.33019	-0.33034	0.34196	0.34282
400	-0.33031	-0.33045	0.34204	0.34291
500	-0.33038	-0.33052	0.34209	0.34296

- (3) In this section, the quantum circuits corresponding to seven steps of SC-ADAPT-VQE were scaled and applied to large lattices with use of the Qiskit MPS circuit simulator. The deviations of the energy density and chiral condensate computed from these wave functions were found to be independent of L , i.e., consistent with $L \leq 14$.

These main points indicate that the quantum circuits determined classically with SC-ADAPT-VQE can be used to prepare the vacuum of the Schwinger model on quantum computers at scale with a precision that is independent of system size.

B. Quantum simulations on 100 qubits using IBM’s quantum computers

The quantum circuits determined via classical simulation on $L \leq 14$ lattices are now scaled to larger L to prepare the vacuum of the Schwinger model on up to 100 qubits of IBM’s 127-superconducting-qubit Eagle quantum computers with heavy-hexagonal communication fabric. Hamiltonian parameters $m = 0.5$ and $g = 0.3$ with $L = 14, 20, 30, 40,$ and 50 , and state preparation circuits scaled from two steps of SC-ADAPT-VQE (compared with seven steps in the previous section), are used. Fewer steps equates to shallower circuits, and a preliminary study of the performance of the computer with more steps can be found in Appendix G. The variational parameters extrapolated to the chosen range of L for two steps of SC-ADAPT-VQE are given in Table XII in Appendix G.

The large number of qubits and two-qubit gates involved in these simulations make error mitigation essential to obtain reliable estimates of observables. Specifically, this work uses readout-error mitigation (REM), dynamical

decoupling (DD), Pauli twirling (PT), and decoherence renormalization. The Qiskit Runtime Sampler primitive is used to obtain readout-corrected quasidistributions via the matrix-free measurement mitigation (M3) from Ref. [147]. Also included in the primitive is DD, which is used to suppress crosstalk and idling errors [148–150]. Crucial to the error mitigation is decoherence renormalization [97,98,106,151], modified in this work for simulations on a large number of qubits, which we call “operator decoherence renormalization.” Underpinning decoherence renormalization is PT [152], which turns coherent two-qubit gate errors into incoherent errors, which can be inverted to recover error-free expectation values. Unlike previous applications of decoherence renormalization, which assume a constant decoherence across the device, ODR estimates the decoherence separately for each operator. This is done by running a mitigation circuit, which has the same operator structure as the one used to extract the observables, but with the noise-free result being known *a priori*. We choose the state preparation circuits with the variational parameters set to zero for mitigation, and in the absence of noise this prepares the strong-coupling vacuum, $|\Omega_0\rangle$ in Eq. (4). Naively, it could be expected that postselecting results on states with total charge $Q = 0$ would eliminate the leading bit-flip errors [100]. However, when postselection is combined with ODR, which accommodates single-qubit decoherence, undesirable correlations between qubits are introduced. We find that performing both mitigation techniques (postselection and ODR) degrades the quality of two-qubit observables, and postselection is not used in this work as it is found to be less effective. More details about ODR and postselection can be found in Appendix E.

The local chiral condensate, χ_j in Eq. (3), obtained from `ibm_cusco` for $L = 50$ is shown in Fig. 7, where the subscript “ j ” denotes the qubit index [153]. Three different

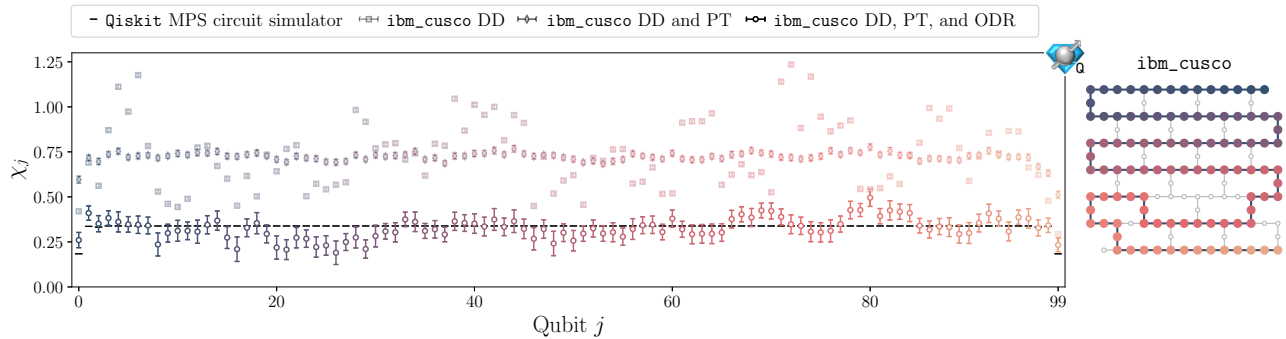


FIG. 7. Local chiral condensate χ_j for $L = 50$, as obtained from IBM’s Eagle-processor quantum computer `ibm_cusco` after different steps of error mitigation: DD (squares), PT (diamonds), and ODR (circles). This is compared with the expected results obtained from the Qiskit MPS circuit simulator (black dashes). Averaging χ_j over all of the qubits (including at the boundaries) gives the chiral condensate presented in Table IV. The layout of the qubits used on the processor is shown on the right. These results were obtained by our performing 150 Pauli twirls, each involving 8×10^3 shots for the physics circuits and the corresponding mitigation circuits. The blue icon in the upper right indicates that this calculation was done on a quantum device [154].

TABLE IV. Chiral condensate in the Schwinger model vacuum obtained from `ibm_brisbane` ($L \leq 40$) and `ibm_cusco` ($L = 50$) for large lattices with $m = 0.5$ and $g = 0.3$ with use of the scaled circuits from two steps of SC-ADAPT-VQE. The values before and after application of ODR are given in columns 4 and 5. Column 6 gives results obtained from our running the two-step SC-ADAPT-VQE circuits on an MPS classical simulator (the noiseless result), while column 7 gives the results from DMRG calculations.

L	Qubits	CNOT gates	$\chi^{(\text{SC-IBM})}$ before ODR	$\chi^{(\text{SC-IBM})}$ after ODR	$\chi^{(\text{SC-MPS})}$	$\chi^{(\text{DMRG})}$
14	28	212	0.491(4)	0.332(8)	0.32879	0.33631
20	40	308	0.504(3)	0.324(5)	0.33105	0.33836
30	60	468	0.513(2)	0.328(4)	0.33319	0.33996
40	80	628	0.532(2)	0.334(3)	0.33444	0.34075
50	100	788	0.721(2)	0.326(3)	0.33524	0.34123

sets of results (in different stages of error mitigation) are shown: with only DD applied (squares), with DD and PT applied (diamonds), and after ODR (circles). Looking at the results with only DD (squares), it is seen that the noise is not uniform across the device, signaling a significant contribution of coherent noise. After PT (diamonds), this coherent noise is averaged out, and is transformed into incoherent (depolarizing) noise, seen by the almost-constant shift of the results compared with the MPS simulation. Finally, ODR removes this shift by mitigating the effects of depolarizing noise. More details on the interplay between these methods can be found in Appendix G.

With the statistics and twirlings gathered, the 1σ uncertainties in each point are approximately 15% of their mean, and each χ_j is within 3σ of the MPS simulator result (the individual values of χ_j can be CP averaged to reduce the uncertainty, as shown in Fig. 14 in Appendix G). It is expected that these uncertainties will reduce with increased statistics and twirlings. Notice that the expected values of χ_j deviate from the volume average for only a few qubits near the boundaries. This is because the boundaries perturb the wave function only over a few correlation lengths, leaving the rest of the volume unaffected. The chiral condensates for $L = 14, 20, 30, 40,$ and 50 are given in Table IV. This is an average over the whole lattice, Eq. (3), and therefore the uncertainty decreases with increasing L due to increased sampling. Despite having smaller uncertainties, the results remain within 3σ of the MPS simulator result. Also given in Table IV is the number of two-qubit CNOT gates. The number of CNOT gates is seen to grow linearly with L , without affecting the quality of the result, and 788 CNOT gates over 100 qubits is well within the capabilities of the quantum computer. This is in line with other quantum simulations that have been performed with large numbers of qubits and CNOT gates using IBM's quantum computers [155–157].

This highlights the fact that it is not the total number of CNOT gates in the quantum circuit that is limiting the scale of simulations, but rather it is the number of CNOT gates per qubit. This, of course, assumes that the CNOT gates in a single layer of the circuit can be enacted in parallel. Because of this, increasing L actually improves volume-averaged quantities by approximately $1/\sqrt{L}$ due

to statistical averaging. In a similar vein, since scalable circuits repeat structures of size ξ many times over the whole lattice, the number of Pauli twirls being sampled is effectively multiplied by L/ξ .

To further probe the quality of the prepared wave functions, correlations between electric charges on the spatial sites are considered. The charge on a spatial site is defined to be the sum of charges on the two associated staggered sites, $\hat{Q}_k = \hat{Q}_{2k} + \hat{Q}_{2k+1}$, where k is an integer corresponding to the spatial site. Of particular interest are connected correlation functions between spatial charges, [158] defined as

$$\langle \hat{Q}_j \hat{Q}_k \rangle_c = \langle \hat{Q}_j \hat{Q}_k \rangle - \langle \hat{Q}_j \rangle \langle \hat{Q}_k \rangle. \quad (11)$$

These correlations decay exponentially for $|j - k| \gtrsim \xi$ due to confinement and charge screening. Unlike the chiral condensate, which is a sum of single-qubit observables, $\langle \hat{Q}_j \hat{Q}_k \rangle_c$ is sensitive to correlations between qubits, i.e., requires measurement of $\langle \hat{Z}_j \hat{Z}_k \rangle$. The results from `ibm_cusco` for $L = 50$ are shown in Fig. 8.

The correlations are symmetric under $j \leftrightarrow k$, and only the lower triangle of the correlation matrix is shown. Each measured value is within 3σ of the MPS simulator result, consistent with statistical fluctuations. Also shown in Fig. 8 are the spatial charge-charge correlations as a function of distance, averaged over the lattice volume,

$$\langle \hat{Q}\hat{Q} \rangle_c(d) = \frac{1}{L-4-d} \sum_{k=2}^{L-3-d} \langle \hat{Q}_k \hat{Q}_{k+d} \rangle_c. \quad (12)$$

To reduce the effects of the boundaries, this sum omits the first and last two spatial lattice sites. As anticipated, this correlation function decays exponentially, with a characteristic length scale proportional to $\xi = 1/m_{\text{hadron}}$ [159]. For $d > 2$, the correlations are consistent with zero within 2σ (note that the log scale distorts the error bars), and increased numbers of shots and twirlings are needed to distinguish additional points from zero. The local chiral condensate and charge-charge correlations corresponding to the other values of L are given in Appendix G.

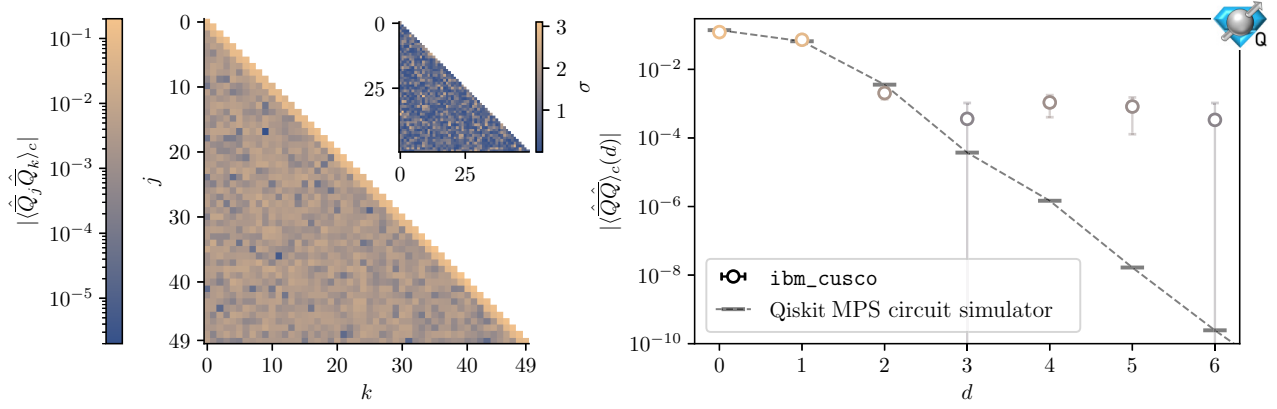


FIG. 8. Left: Connected contributions to the spatial charge-charge correlation functions, $\langle \hat{Q}_j \hat{Q}_k \rangle_c$, for $L = 50$ (the inset shows the number of standard deviations by which the results obtained from `ibm_cusco` deviate from the MPS simulator results). Right: Volume-averaged correlation functions as a function of distance d , $\langle \hat{Q} \hat{Q} \rangle_c(d)$, with the points following the same color map as in the left main panel (error bars show 1σ standard deviations).

VI. SUMMARY AND OUTLOOK

In this work, the vacuum of the lattice Schwinger model was prepared on up to 100 qubits of IBM’s 127-qubit Eagle-processor quantum computers, `ibm_brisbane` and `ibm_cusco`. This was accomplished with SC-ADAPT-VQE, an algorithm for identifying systematically improvable state preparation quantum circuits that can be robustly scaled to operate on any number of qubits. The utility of scalable circuits relies on physically relevant systems often having a (discrete) translational symmetry, and a finite correlation length set by the mass gap. Together, these imply that the state preparation circuits have unique structure over approximately a correlation length [107,108], which is replicated across the lattice. The lattice Schwinger model with OBCs was chosen to explore these ideas as its vacuum has (approximate) translational invariance and, due to confinement, has a mass gap. By performing SC-ADAPT-VQE on a classical simulator, we built state preparation circuits for lattices of $L \leq 14$ (28 qubits) from an operator pool containing both translationally invariant terms and ones localized to the boundaries. Exponential convergence in the quality of the prepared state with both system size and circuit depth enabled the extrapolation of circuits that can be scaled to arbitrarily large lattices. This methodology was successfully demonstrated by our preparing the Schwinger model vacuum on up to 100 superconducting qubits of IBM’s quantum computers. Both the charge-charge correlators and the chiral condensate were measured, and were found to agree with results from an MPS simulator, within statistical uncertainty. Vital to the success of these quantum simulations involving a large number of qubits was the development of an improved error-mitigation technique, which we have called “operator decoherence renormalization.”

Because of its generality, we expect that the scalable circuit framework embodied by SC-ADAPT-VQE can be applied to other gapped theories with translationally invariant ground states. Of particular importance is QCD, for which the initialization of ground states for quantum simulations continues to be a daunting prospect. It is likely that many of the ideas used to construct efficient state preparation circuits for the Schwinger model can be applied to the initialization of the ground state of QCD. Of course, the operator pool that informs the state preparation circuits will be more diverse since the gauge field is no longer completely constrained by Gauss’s law. Local quark-field operators, extended quark operators with associated gauge links, and closed loops of gauge links will need to be included in the pool. It is also expected that the variational parameters defining the ground-state preparation circuits will converge exponentially, once the simulation volume can completely contain the pion(s).

The utility of SC-ADAPT-VQE is that it provides a straightforward prescription for determining low-depth quantum circuits that prepare the ground state on systems of arbitrary size with only classical computing overhead. This not only allows the quantum simulation of ground state properties, but will be important for future simulations of dynamics, where preparing the initial state is a crucial first step. Scalable circuits can likely be used to prepare single-hadron and multihadron states, for example, a vector meson in the Schwinger model or a baryon in QCD. Once these states are initialized, they can be used to simulate scattering and electroweak processes and to probe properties of dense matter. As an example, localized e^+e^- pairs on top of the Schwinger model vacuum could be prepared and evolved forward in time. Such localized distributions can have high-energy components, whose propagation through the lattice leaves behind showers of

particles. These processes probe the dynamics of fragmentation, confinement, and hadron production, and lead to long-range correlations that entangle distant regions of the lattice (see, e.g., Refs. [68,92,160,161]). As simulations of highly entangling dynamics at scale are beyond the capabilities of classical computing, they are a candidate for an early quantum advantage for scientific applications.

ACKNOWLEDGMENTS

We thank Caroline Robin for interesting discussions and reading the manuscript, and Sophia Economou for interesting discussions about ADAPT-VQE and symmetries. We also thank the participants of the Quantum Error Mitigation for Particle and Nuclear Physics IQuS-INT workshop held between May 9 and 13, 2022, for helpful discussions. R.C.F. thanks the organizers of the Quantum Connections summer school, where some of this work was performed. This work was supported, in part, by U.S. Department of Energy Grant No. DE-FG02-97ER-41014 (R.C.F.), by the U.S. Department of Energy, Office of Science, Office of Nuclear Physics, Inqubator for Quantum Simulation under Award No. DOE (NP) Award DE-SC0020970 via the Quantum Horizons: QIS Research and Innovation for Nuclear Science program (A.N.C, R.C.F, and M.J.S), and by the Quantum Science Center, a National Quantum Information Science Research Center of the U.S. Department of Energy (M.I.). This work was also supported, in part, through the Department of Physics and the College of Arts and Sciences at the University of Washington. This research used resources of the Oak Ridge Leadership Computing Facility, which is a U.S. Department of Energy, Office of Science user facility supported under Contract No. DE-AC05-00OR22725. We acknowledge the use of IBM Quantum services for this work. This work was enabled, in part, by the use of advanced computational, storage, and networking infrastructure provided by the Hyak supercomputer system at the University of Washington. We have made extensive use of Wolfram MATHEMATICA [162], PYTHON [163,164], JULIA [165], and JUPYTER NOTEBOOKS [166] in the CONDA environment [167], and IBM's quantum programming environment Qiskit [138]. The DMRG calculations were performed with use of the C++ ITensor library [168].

The views expressed are those of the authors, and do not reflect the official policy or position of IBM or the IBM Quantum team.

APPENDIX A: THE SCHWINGER MODEL HAMILTONIAN IN THE $Q = 0$ SECTOR

In the absence of background electric charges, the lowest-energy sector of the Schwinger model has vanishing charge, $Q = \sum_n Q_n = 0$. Restriction to this sector permits a simplification of the Hamiltonian, reducing the

number of terms appearing in the electric contribution:

$$\hat{H}_{el} \stackrel{Q=0}{=} \frac{g^2}{2} \left\{ \sum_{n=0}^{L-1} (L-n) \left[\hat{Q}_n^2 + (1 - \delta_{n0}) \hat{Q}_{2L-n}^2 \right] + 2 \sum_{n=0}^{L-1} \left[\sum_{m=n+1}^{L-1} (L-m) \hat{Q}_m \hat{Q}_n + \sum_{m=1}^{n-1} (L-n) \hat{Q}_{2L-m} \hat{Q}_{2L-n} \right] \right\}. \quad (\text{A1})$$

This reduces the number of $\hat{Q}_n \hat{Q}_m$ terms from $1 - 3L + 2L^2$ to $1 + L^2 - 2L$ and the required connectivity from all-to-all to half-to-half. Note that this can also be used to simplify the $(1+1)\text{D}$ $SU(N)$ Hamiltonian in the $Q_n^{(a)} = 0$ (color singlet) sector, by replacing $\hat{Q}_n \rightarrow \hat{Q}_n^{(a)}$ with $a \in \{1, 2, \dots, N^2 - 1\}$.

Further simplifications to this Hamiltonian are likely possible by taking advantage of the exponential decay of correlations between spatial charges \hat{Q} separated by distance $d > \xi$. This will allow the construction of a truncated \hat{H}_{el} that has only $\mathcal{O}(L\xi)$ terms. In addition, such a Hamiltonian will require connectivity only between qubits separated by $d \lesssim \xi$ instead of $d \leq L$.

APPENDIX B: VOLUME EXTRAPOLATION OF THE ENERGY DENSITY AND CHIRAL CONDENSATE

Here the vacuum energy density and chiral condensate are extrapolated to $L = \infty$. The results of exact diagonalization and DMRG calculations are considered independently, providing consistent results within uncertainties. For the DMRG calculations, 60 sweeps were performed with a maximum allowed bond dimension of 150 and a truncation of Schmidt coefficients below 10^{-10} . This showed a convergence of 10^{-10} in the energy of the vacuum state. Discussions in Sec. II A about boundary effects motivated an inverse-power, $1/L$, dependence of the exact vacuum energies as the infinite-volume limit is approached. This scaling was argued when L is much larger than the longest correlation length, and with OBCs. Therefore, for masses and couplings that give rise to the lowest-lying hadron being completely contained within the lattice volume, we anticipate functional forms

$$\begin{aligned} \varepsilon(L) &= \varepsilon(\infty) + \frac{e_1}{L} + \mathcal{O}\left(\frac{1}{L^2}\right), \\ \chi(L) &= \chi(\infty) + \frac{d_1}{L} + \mathcal{O}\left(\frac{1}{L^2}\right) \end{aligned} \quad (\text{B1})$$

for ε and χ . This is due to the finite penetration depth of boundary effects, and the exponential convergence of both

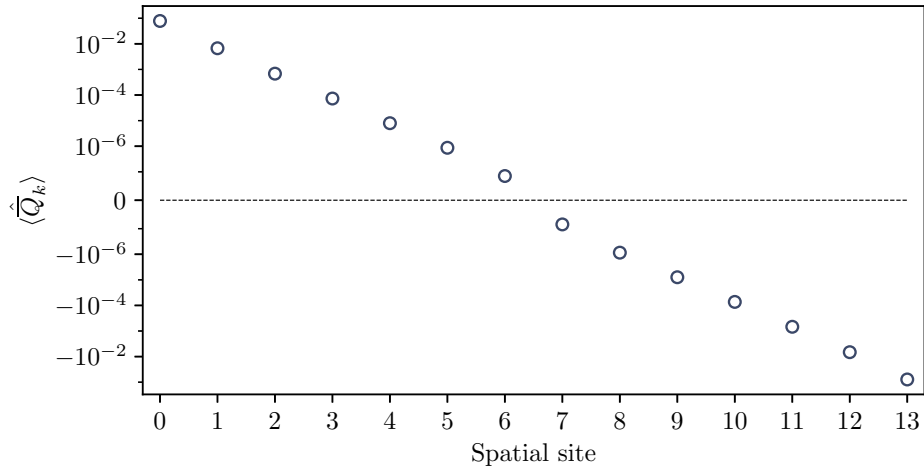


FIG. 9. Charge on each spatial site, $\langle \hat{Q}_k \rangle$, for $m = 0.5$, $g = 0.3$, and $L = 14$ obtained from exact diagonalization of the Hamiltonian.

the volume and the surface contributions to their infinite-volume values. As a result, the surface terms make $\mathcal{O}(1/L)$ contributions to intensive quantities, e.g., densities. To illustrate this, the expectation value of the charge on each spatial site, $\langle \hat{Q}_k \rangle$, for $m = 0.5$, $g = 0.3$, and $L = 14$ is shown in Fig. 9. This converges exponentially with the distance to the boundary to $\langle \hat{Q}_k \rangle = 0$, the expected infinite-volume value.

The results of fits to the exact and DMRG results for the energy density and chiral condensate for $m = 0.5$ and $g = 0.3$ are shown in Fig. 2 and for $m = 0.1$ and $g = 0.8$ and for $m = 0.1$ and $g = 0.3$ are shown in Fig. 10. Using polynomials that are linear and quadratic in $1/L$, we performed fits for $L \geq 9$ and extrapolated to $L = \infty$. The differences between extrapolations obtained from the two fit forms are used to estimate the systematic fitting error, corresponding to the black and gray points (and error bars).

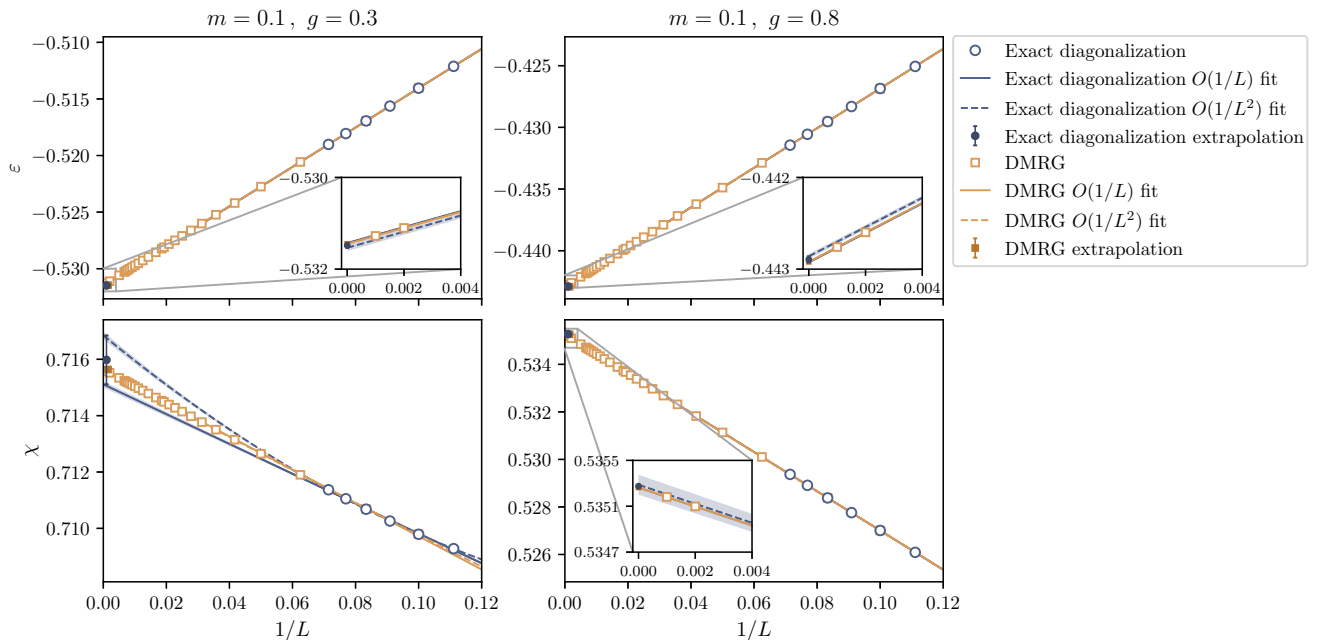


FIG. 10. L extrapolations of the vacuum energy density ε (top) and chiral condensate χ (bottom) for $m = 0.1$ and $g = 0.3$ (left) and $m = 0.1$ and $g = 0.8$ (right). Each panel shows extrapolations of the exact values given in Tables VII and IX (blue circles) and of the results from DMRG calculations (orange squares) given in Table V for $L \geq 9$. The solid lines correspond to linear extrapolations and the dashed lines correspond to quadratic extrapolations, and are found to overlap (see the insets). The darker points show the $L = \infty$ extrapolated value, with an uncertainty determined by the difference between the linear and quadratic extrapolations.

TABLE V. Additional results for the energy density ε and chiral condensate χ obtained from DMRG calculations, and used in the extrapolations in Figs. 2 and 10.

L	$m = 0.1, g = 0.3$		$m = 0.1, g = 0.8$		$m = 0.5, g = 0.3$	
	$\varepsilon^{(\text{DMRG})}$	$\chi^{(\text{DMRG})}$	$\varepsilon^{(\text{DMRG})}$	$\chi^{(\text{DMRG})}$	$\varepsilon^{(\text{DMRG})}$	$\chi^{(\text{DMRG})}$
10	-0.51405	0.70979	-0.42685	0.52701	-0.31707	0.33358
12	-0.51694	0.71068	-0.42953	0.52838	-0.31936	0.33517
16	-0.52057	0.71190	-0.43288	0.53010	-0.32221	0.33716
20	-0.52275	0.71265	-0.43488	0.53114	-0.32393	0.33836
24	-0.52420	0.71315	-0.43622	0.53182	-0.32508	0.33916
28	-0.52523	0.71350	-0.43718	0.53232	-0.32589	0.33973
32	-0.52601	0.71377	-0.43790	0.53268	-0.32650	0.34016
36	-0.52661	0.71398	-0.43846	0.53297	-0.32698	0.34049
40	-0.52710	0.71414	-0.43890	0.53320	-0.32736	0.34075
44	-0.52749	0.71428	-0.43927	0.53339	-0.32768	0.34097
48	-0.52782	0.71439	-0.43957	0.53354	-0.32794	0.34115
52	-0.52810	0.71449	-0.43983	0.53368	-0.32816	0.34130
54	-0.52823	0.71453	-0.43994	0.53374	-0.32825	0.34137
60	-0.52855	0.71464	-0.44024	0.53389	-0.32851	0.34155
70	-0.52896	0.71479	-0.44062	0.53408	-0.32883	0.34178
80	-0.52927	0.71489	-0.44091	0.53423	-0.32908	0.34195
90	-0.52952	0.71498	-0.44113	0.53435	-0.32927	0.34208
100	-0.52971	0.71504	-0.44131	0.53444	-0.32942	0.34219
110	-0.52987	0.71510	-0.44146	0.53451	-0.32955	0.34228
120	-0.53000	0.71514	-0.44158	0.53458	-0.32965	0.34235
130	-0.53011	0.71518	-0.44168	0.53463	-0.32974	0.34241
140	-0.53021	0.71521	-0.44177	0.53467	-0.32981	0.34246
150	-0.53029	0.71524	-0.44185	0.53471	-0.32988	0.34251
200	-0.53058	0.71534	-0.44212	0.53485	-0.33011	0.34267
500	-0.53110	0.71552	-0.44260	0.53510	-0.33052	0.34295
1000	-0.53128	0.71558	-0.44276	0.53518	-0.33066	0.34305

The difference between linear and quadratic fits is negligible for the exact results, except for the chiral condensate in the case of $m = 0.1$ and $g = 0.3$, which sees a small quadratic dependence. When the fit interval is reduced to $L \geq 10$, this dependence once again becomes negligible.

APPENDIX C: OPTIMIZING TROTTERIZED CIRCUITS FOR STATE PREPARATION

As discussed in the main text, even after the operator pool has been chosen for SC-ADAPT-VQE, there remains freedom in how the pool of unitary operators, Eq. (5), is implemented as quantum circuits. For example, instead of leading-order Trotterization, a higher-order Trotterization could be used to suppress Trotter errors. Alternatively, different orderings of the terms in the leading-order Trotterization can be considered. This freedom can be used to optimize the convergence of SC-ADAPT-VQE with circuit depth. Also, different Trotter orderings can break the CP symmetry. The circuit orderings in Fig. 4 were chosen to minimize the circuit depth, and for $d = 1, 3, 5$ this ordering preserves CP symmetry, while for $d = 7, 9$ it breaks CP symmetry.

Consider the different arrangements of the terms in the Trotterization of $\hat{O}_{mh}^V(1)$, given in Eq. (8), as shown in Fig. 11(a). The depth-2 ordering (left) was used to obtain the results presented in the main text as it leads to the shallowest circuits. All the orderings shown in Fig. 11(a) are equivalent up to $\mathcal{O}[(\theta_1)^2]$ (where θ_1 is the coefficient of the operator in the corresponding unitary operator), but the deeper circuits allow the generation of longer-range correlations. Note that the deeper circuits can break the CP symmetry; e.g., for $L = 10$ depths 2 and 4 preserve CP symmetry while depths 3, 4, 5, and 7 break CP symmetry. It is found that this added circuit depth improves the convergence of SC-ADAPT-VQE, as shown in Fig. 11(b). This demonstrates that to minimize circuit depth, for a fixed error threshold, it is preferable to choose a deeper Trotterization of $\hat{O}_{mh}^V(1)$, instead of going to a greater number of SC-ADAPT-VQE steps. For example, it is more efficient to perform two steps of SC-ADAPT-VQE with a depth-3 Trotterization of $\hat{O}_{mh}^V(1)$ than to perform three steps of SC-ADAPT-VQE with a depth-2 Trotterization of $\hat{O}_{mh}^V(1)$. Also shown in Fig. 11(b) are results obtained from our performing SC-ADAPT-VQE with exact unitary operators (no Trotterization). This is found to always perform better than the Trotterized unitaries, except for a single

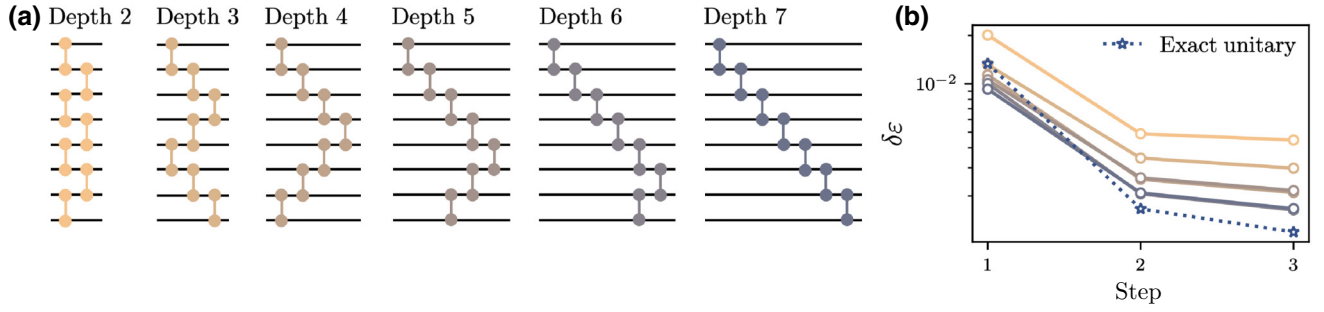


FIG. 11. (a) Orderings of Trotterized terms for implementing $\hat{O}_{mh}^V(1)$. Circuits of depth 2–7 are shown from left to right, with the dumbbells representing the circuit in Fig. 3(a). (b) Deviations in the energy density of the SC-ADAPT-VQE prepared state for $m = 0.5, g = 0.3$, and $L = 10$ with different depth implementations of the Trotterization of $\hat{O}_{mh}^V(1)$.

step. Intriguingly, for a single step, the error is less with a deep first-order Trotterization than with the exact unitary. This suggests that the optimizer is finding a solution in which the Trotter errors are tuned to improve the overlap with the vacuum. Note that the deeper Trotterizations of $\hat{O}_{mh}^V(1)$ move the recurrence of $\hat{O}_{mh}^V(1)$ (e.g., at step 4 for $m = 0.5$ and $g = 0.3$) to deeper in the SC-ADAPT-VQE ansatz.

APPENDIX D: VOLUME EXTRAPOLATIONS OF THE SC-ADAPT-VQE VARIATIONAL PARAMETERS: AN “EFFECTIVE θ_i^∞ ”

To initialize large quantum registers, the variational parameters defining the state preparation quantum circuits need to be extrapolated with high precision. In volumes large enough to contain the longest correlation length, the variational parameters are expected to be exponentially

close to their infinite-volume values. Therefore, we assume that the form of the volume dependence for practical purposes is that given in Eq. (10),

$$\theta_i(L) = \theta_i^\infty + c_1 e^{-c_2 L}, \quad (\text{D1})$$

and check the self-consistency of this form [169]. While there could be a polynomial coefficient of the exponential, we find that this is not required. Fitting exponential functions can be challenging; however, with results over a sufficient range of L , algebraic techniques, such as effective masses, have proven useful in lattice QCD calculations to eliminate “uninteresting” parameters, while at the same time mitigating correlated fluctuations in measurements [170–174]. With the goal of initializing large lattices, it is the θ_i^∞ that are of particular interest.

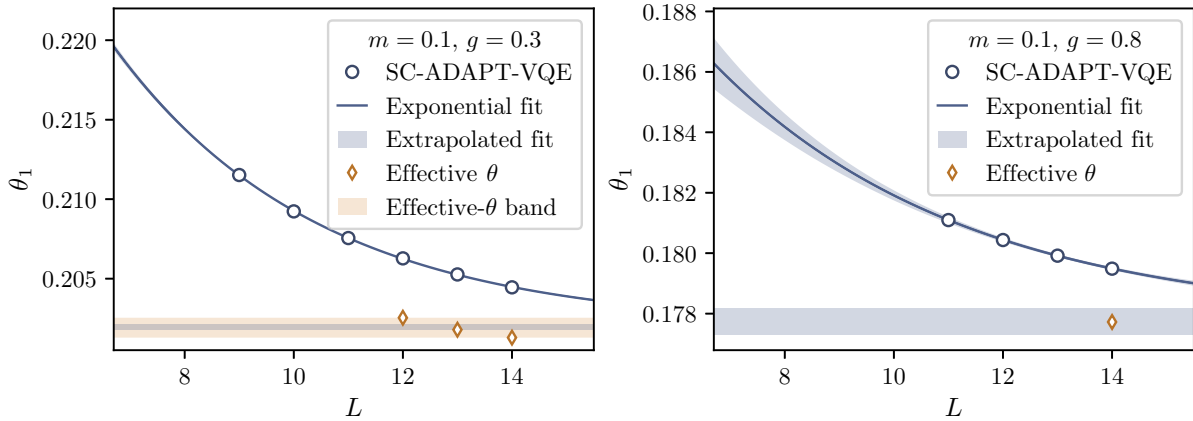


FIG. 12. Further examples of fitting the asymptotic L dependence of the variational parameters defining the state preparation quantum circuit, determined from classical simulations using SC-ADAPT-VQE. The results for $\theta_1 = \hat{O}_{mh}^V(1)$ (blue points) for $m = 0.1$ and $g = 0.3$ (left panel) given in Table VI and for $m = 0.1$ and $g = 0.8$ (right panel) given in Table VIII are extrapolated to $L = \infty$ by (i) use of a three-parameter fit given in Eq. (10), as shown by the blue line and shaded region, with an asymptotic value shown by the gray region, and by (ii) the forming of effective θ (orange diamonds), with the maximum and minimum values shown as the orange shaded region (where possible).

Assuming the volume dependence given in Eq. (D1), it is useful to form four relations:

$$\begin{aligned}
 y_L &= \theta_i(L) - \theta_i^\infty = c_1 e^{-c_2 L}, \\
 y_{L+1} &= \theta_i(L+1) - \theta_i^\infty = c_1 e^{-c_2} e^{-c_2 L} \\
 y_{L+2} &= \theta_i(L+2) - \theta_i^\infty = c_1 e^{-2c_2} e^{-c_2 L}, \\
 y_{L+3} &= \theta_i(L+3) - \theta_i^\infty = c_1 e^{-3c_2} e^{-c_2 L}. \quad (\text{D2})
 \end{aligned}$$

These relations can be combined to isolate θ_i^∞ , providing an L -dependent ‘‘effective θ_i^∞ ’’, denoted as $\theta_{i,\text{eff}}^\infty$:

$$\begin{aligned}
 y_{L+1}y_{L+2} &= y_L y_{L+3}, \\
 \theta_{i,\text{eff}}^\infty(L) &= \frac{\theta_i(L)\theta_i(L+3) - \theta_i(L+1)\theta_i(L+2)}{\theta_i(L) + \theta_i(L+3) - \theta_i(L+1) - \theta_i(L+2)}. \quad (\text{D3})
 \end{aligned}$$

For a sufficiently large set of results, $\theta_{i,\text{eff}}^\infty(L)$ will plateau for large L if the functional form in Eq. (D1) correctly describes the results. This plateau can be fit by a constant, over some range of large L , to provide an estimate of θ_i^∞ . This method is similar to using varpro (variable projection) in a multiparameter χ^2 minimization.

As an example, the results for θ_1^∞ from a three-parameter fit of θ_1 to Eq. (D1) are compared with a determination using $\theta_{1,\text{eff}}^\infty(L)$ from Eq. (D3). Results obtained with these two methods for $m = 0.1$ and $g = 0.3$ and for $m = 0.1$ and $g = 0.8$ are shown in Fig. 12.

The result obtained from fitting a constant to $\theta_{1,\text{eff}}^\infty(L)$ is consistent with the asymptotic result from the three-parameter fit, but with somewhat larger uncertainty. The current deficiency of this comparison is the small number of points in the plateau region, and results for larger L are required for a more comprehensive comparison. Analysis of the other variational parameters shows a similar behavior.

The consistency between the two extraction methods is encouraging, and suggests that the selected exponential form may indeed well describe the results. The fitting method is likely insensitive to polynomial corrections (coefficients), and requires further exploration to fully quantify uncertainties in these asymptotic values of the variational parameters. However, as the MPS simulations with these extrapolated angles reproduce the results obtained with DMRG calculations, it appears that, for the systems and parameters we have selected in our analysis, systematic errors introduced by selecting this functional form are small.

APPENDIX E: OPERATOR DECOHERENCE RENORMALIZATION

To mitigate the effects of noise, the decoherence renormalization technique [97,98,106,151] is modified for use with larger systems. In its original form, decoherence renormalization assumes that each qubit decoheres at the same rate under a depolarizing noise channel. When one is working with a small number of qubits, this is a reasonable approximation, but for larger systems, it is necessary to consider the rate of decoherence of each qubit individually. After Pauli twirling, the qubit errors are well described by a Pauli error channel [175], which maps the N -qubit density matrix to

$$\rho \rightarrow \sum_{i=1}^{4^N} \eta_i \hat{P}_i \rho \hat{P}_i, \quad (\text{E1})$$

where \hat{P}_i is a tensor product of Pauli operators (\hat{I} , \hat{X} , \hat{Y} , or \hat{Z}) acting on N qubits, and the set of η_i characterizes the error channel. It is important to understand the effect of this error channel on observables. Generic observables can be written as a sum over tensor products of Pauli operators, so it suffices to consider an observable, \hat{O} , that is a tensor product of Pauli operators. Under a Pauli error channel, the

TABLE VI. Same as Table II except for $m = 0.1$ and $g = 0.3$.

L	θ_i								
	$\hat{O}_{mh}^V(1)$	$\hat{O}_{mh}^V(3)$	$\hat{O}_{mh}^V(5)$	$\hat{O}_{mh}^V(1)$	$\hat{O}_{mh}^V(7)$	$\hat{O}_{mh}^V(9)$	$\hat{O}_{mh}^S(0,1)$	$\hat{O}_{mh}^V(9)$	$\hat{O}_{mh}^V(1)$
6	0.25704	-0.11697	0.04896	0.18116	-0.02664	—	0.19193	0.01539	—
7	0.25796	-0.11580	0.04776	0.18099	-0.02471	0.01250	0.18971	—	—
8	0.25862	-0.11507	0.04711	0.18087	-0.02380	0.01155	0.18832	—	—
9	0.21152	-0.11560	0.04859	0.12687	-0.02419	0.01162	—	—	0.11093
10	0.20923	-0.11491	0.04809	0.12749	-0.02368	0.01122	—	—	0.11182
11	0.20755	-0.11437	0.04771	0.12792	-0.02331	0.01093	—	—	0.11244
12	0.20628	-0.11393	0.04741	0.12823	-0.02303	0.01072	—	—	0.11289
13	0.20526	-0.11357	0.04716	0.12846	-0.02280	0.01056	—	—	0.11324
14	0.20445	-0.11328	0.04696	0.12863	-0.02262	0.01044	—	—	0.11352
∞	0.202	-0.112	0.046	0.129	-0.022	0.010	—	—	0.114

TABLE VII. Same as Table I except for $m = 0.1$ and $g = 0.3$.

L	$\varepsilon^{(\text{aVQE})}$	$\varepsilon^{(\text{exact})}$	$\chi^{(\text{aVQE})}$	$\chi^{(\text{exact})}$	\mathcal{I}_L	CNOT gates per qubit
6	-0.49927	-0.50256	0.68192	0.70834	0.00377	38
7	-0.50350	-0.50663	0.68442	0.70837	0.00337	44.3
8	-0.50670	-0.50971	0.68653	0.70877	0.00309	48.8
9	-0.50838	-0.51212	0.68694	0.70928	0.00449	53.7
10	-0.51057	-0.51405	0.68902	0.70979	0.00412	56.1
11	-0.51236	-0.51563	0.69073	0.71026	0.00382	58.1
12	-0.51385	-0.51694	0.69217	0.71068	0.00358	59.8
13	-0.51512	-0.51806	0.69340	0.71105	0.00337	61.2
14	-0.51620	-0.51902	0.69445	0.71137	0.00319	62.4

measured (noisy) expectation value, $\langle \hat{O} \rangle_{\text{meas}}$, is given by

$$\langle \hat{O} \rangle_{\text{meas}} = \sum_{i=1}^{4^N} \eta_i \text{Tr}(\hat{P}_i \hat{O} \hat{P}_i \rho). \quad (\text{E2})$$

Note that $\hat{P}_i \hat{O} \hat{P}_i = \pm \hat{O}$, depending on whether or not \hat{O} and \hat{P}_i commute or anticommute. On this basis, the measured (noisy) expectation value, $\langle \hat{O} \rangle_{\text{meas}}$, can be seen to be directly proportional to the predicted (noiseless) expectation value, $\langle \hat{O} \rangle_{\text{pred}} = \text{Tr}(\hat{O} \rho)$, i.e.,

$$\langle \hat{O} \rangle_{\text{meas}} = (1 - \eta_O) \langle \hat{O} \rangle_{\text{pred}}. \quad (\text{E3})$$

The ODR factor η_O is, in general, distinct for each operator, and can be estimated by running a mitigation circuit that has the same structure as the physics circuit, but where $\langle \hat{O} \rangle_{\text{pred}}$ is already known. In this work, the mitigation circuit was taken to be the state preparation circuit with variational parameters set to zero, which is the identity in the absence of noise. This mitigation circuit will have the same noise channel as the physics circuit provided that the noise is dominated by errors in the two-qubit gates and is independent of the single-qubit rotation angles in the circuit. Without noise, the mitigation circuit prepares

the strong-coupling vacuum, where $\langle \hat{O} \rangle_{\text{pred}}$ is known, and therefore η_O can be computed. Once η_O is determined, Eq. (E3) is used to estimate the value of the noiseless observable from the results of the physics circuits.

An added benefit of ODR is that it reduces the need for other error-mitigation techniques. For example, readout errors are partially mitigated since the measured observables are affected by both gate and measurement errors. This is convenient as current measurement mitigation techniques require a large classical computing overhead. It also reduces the need for postselection, which in our work could have been performed on states with total charge $Q = 0$. This postselection removes single-qubit errors, but introduces further correlations between qubits. These correlations effectively increase the size of the single-qubit errors (making observables sensitive to errors anywhere on the register). This reduces the efficacy of the Pauli error model, making postselection incompatible with ODR [176]. Another desirable feature of ODR is that it allows simulations to retain the results of a much larger fraction of the ensemble. This is because the probability of a single-qubit error increases with system size, and therefore much of the ensemble is lost with naive postselection. Further, such errors have little effect on local observables that are summed across the entire qubit register.

TABLE VIII. Same as Table II except with $m = 0.1$ and $g = 0.8$ and through six steps of the SC-ADAPT-VQE algorithm.

L	θ_i						
	$\hat{O}_{mh}^V(1)$	$\hat{O}_{mh}^V(3)$	$\hat{O}_{mh}^V(5)$	$\hat{O}_{mh}^V(1)$	$\hat{O}_{mh}^V(7)$	$\hat{O}_{mh}^S(0,1)$	$\hat{O}_{mh}^V(1)$
6	0.22698	-0.06357	0.01441	0.15594	-0.00418	0.14247	-
7	0.22784	-0.06303	0.01416	0.15559	-0.00395	0.14111	-
8	0.22843	-0.06267	0.01401	0.15535	-0.00382	0.14018	-
9	0.22885	-0.06240	0.01390	0.15518	-0.00374	0.13951	-
10	0.22918	-0.06219	0.01382	0.15505	-0.00368	0.13900	-
11	0.18110	-0.06192	0.01431	0.11095	-0.00377	-	0.09796
12	0.18044	-0.06169	0.01423	0.11108	-0.00372	-	0.09809
13	0.17992	-0.06151	0.01416	0.11116	-0.00369	-	0.09819
14	0.17949	-0.06135	0.01410	0.11124	-0.00366	-	0.09825
∞	0.178	-0.061	0.014	0.112	-0.004	-	0.098

TABLE IX. Same as Table I except with $m = 0.1$ and $g = 0.8$ and through six steps of the SC-ADAPT-VQE algorithm.

L	$\varepsilon^{(\text{aVQE})}$	$\varepsilon^{(\text{exact})}$	$\chi^{(\text{aVQE})}$	$\chi^{(\text{exact})}$	\mathcal{I}_L	CNOT gates per qubit
6	-0.41488	-0.41614	0.51372	0.52154	0.00072	29.5
7	-0.41869	-0.41996	0.51579	0.52348	0.00071	32.1
8	-0.42156	-0.42283	0.51736	0.52495	0.00071	33.9
9	-0.42379	-0.42506	0.51859	0.52609	0.00071	35.2
10	-0.42557	-0.42685	0.51958	0.52701	0.00071	36.3
11	-0.42669	-0.42831	0.51945	0.52776	0.00129	38.9
12	-0.42799	-0.42953	0.52047	0.52838	0.00121	39.7
13	-0.42909	-0.43056	0.52134	0.52891	0.00115	40.3
14	-0.43003	-0.43144	0.52209	0.52937	0.00109	40.9

APPENDIX F: ADDITIONAL RESULTS FROM CLASSICAL SIMULATIONS

The results corresponding to Fig. 5 for $m = 0.1$ and $g = 0.3$ are given in Tables VI and VII and for $m = 0.1$ and $g = 0.8$ are given in Tables VIII and IX. The sixth step of the algorithm is chosen for $m = 0.1$ and $g = 0.8$ because the operator structure through $L = 14$ has converged, allowing a consistent extrapolation of the circuits to large L . This can be seen by comparing the operator structure in Table VIII (six steps) and the operator structure in Table X (seven steps). An interesting observation is that the sum of parameters for a particular operator in the ansatz remains approximately unchanged when an additional insertion of the operator is added. For example, compare the sum of parameters for $\hat{O}_{mh}^V(1)$ between $L = 8$ and $L = 9$ in Table VI. Using the same method as for $m = 0.5$ and $g = 0.3$ in Sec. IV, we also determined scalable circuits for $m = 0.1$ and $g = 0.3$ and for $m = 0.1$ and $g = 0.8$. The results of running these circuits on Qiskit's MPS simulator for $m = 0.1$ and $g = 0.3$ and for $m = 0.1$ and $g = 0.8$ are given in Table XI. Because of the longer correlation lengths for these parameters, it was not possible to go to $L = 500$ with the available computing resources. In these MPS simulations, Qiskit's default settings were used, where the bond dimension increases until machine precision is achieved. The details of the Qiskit MPS simulator can be found on the Qiskit website [177]. Again,

the energy density and chiral condensate are found to have precision comparable to that found on smaller systems. This shows that, despite the longer correlation lengths for $m = 0.1$ and $g = 0.3$ and for $m = 0.1$ and $g = 0.8$, it is still possible to accurately extrapolate the state preparation circuits to large lattices. Note that stabilization of operator ordering for the different m and g (see Tables II, VI, and X) does not follow the hierarchy in correlation lengths. This is because larger ξ increases the contribution of the volume (approximately $e^{-d/\xi}$) and the surface (approximately ξ/L) terms to the energy density.

To emphasize the advantage of performing SC-ADAPT-VQE using a classical simulator, we give an estimate of the number of shots required to perform SC-ADAPT-VQE on a quantum computer. For $m = 0.5$, $g = 0.3$, and $L = 14$, our performing ten steps of SC-ADAPT-VQE required approximately 6000 calls to the optimizer, in addition to about 500 evaluations of $\langle [\hat{H}, \hat{O}_i] \rangle$ for pool operators \hat{O}_i . Each one of these calls required roughly 10^{-3} precision in the measured observable, corresponding to about 10^6 shots on a noiseless device. Therefore, SC-ADAPT-VQE for $L = 14$ would require approximately 10^{10} shots on a noiseless device. If the effects of device noise are factored in, this estimate would increase by at least a factor of 10, and probably close to a 1×10^{12} shots would be required to perform SC-ADAPT-VQE on a quantum computer. This is infeasible on current hardware.

 TABLE X. Same as Table I except with $m = 0.1$ and $g = 0.8$ and through seven steps of the SC-ADAPT-VQE algorithm.

L	θ_i								
	$\hat{O}_{mh}^V(1)$	$\hat{O}_{mh}^V(3)$	$\hat{O}_{mh}^V(5)$	$\hat{O}_{mh}^V(1)$	$\hat{O}_{mh}^V(7)$	$\hat{O}_{mh}^S(0,1)$	$\hat{O}_{mh}^V(1)$	$\hat{O}_{mh}^S(0,1)$	$\hat{O}_{mh}^V(9)$
6	0.17222	-0.06236	0.01456	0.11495	-0.00409	0.07017	0.09561	-	-
7	0.17278	-0.06184	0.01433	0.11431	-0.00389	0.06947	0.09620	-	-
8	0.17316	-0.06147	0.01417	0.11388	-0.00378	0.06900	0.09659	-	-
9	0.17344	-0.06121	0.01407	0.11357	-0.00371	0.06866	0.09688	-	-
10	0.17365	-0.06101	0.01399	0.11333	-0.00366	0.06840	0.09710	-	-
11	0.17300	-0.06058	0.01385	0.11216	-0.00359	-	0.09885	0.07047	-
12	0.17321	-0.06048	0.01381	0.11210	-0.00357	-	0.09883	0.07028	-
13	0.17338	-0.06039	0.01378	0.11205	-0.00355	-	0.09883	0.07012	-
14	0.17950	-0.06139	0.01417	0.11124	-0.00382	-	0.09825	-	0.00107

TABLE XI. Same as Table III except with $m = 0.1$ and $g = 0.3$ and with $m = 0.1$ and $g = 0.8$.

L	$\varepsilon^{(\text{SC-MPS})}$	$\varepsilon^{(\text{DMRG})}$	$\chi^{(\text{SC-MPS})}$	$\chi^{(\text{DMRG})}$
$m = 0.1, g = 0.3$				
50	-0.52640	-0.52797	0.70967	0.71444
100	-0.52838	-0.52971	0.71359	0.71504
$m = 0.1, g = 0.8$				
50	-0.43886	-0.43971	0.53339	0.53361
100	-0.44058	-0.44131	0.53604	0.53444
200	-0.44144	-0.44212	0.53737	0.53485
300	-0.44173	-0.442384	0.53781	0.53499
400	-0.44187	-0.44252	0.53803	0.53506

APPENDIX G: ADDITIONAL DETAILS AND RESULTS FROM SIMULATIONS USING IBM'S QUANTUM COMPUTERS

In this appendix, we provide additional details about how our results are obtained from IBM's quantum computers, together with the additional figures not shown in Sec. VB. All measurements are performed on `ibm_brisbane` ($L \leq 40$) and `ibm_cusco` ($L = 50$) by our sending the state preparation circuits, with measurements in the computational (z) basis, via the Qiskit Runtime Sampler primitive. The values of the variational parameters obtained from fitting to the exponential form in Eq. (10) for two steps of SC-ADAPT-VQE are given in Table XII. The different qubits used for each lattice size can be seen in the insets in Figs. 7 and 13. χ_j , obtained from `ibm_brisbane` for $L = 14, 20, 30$, and 40, is shown in Fig. 13, and the charge-charge correlation functions are shown in Fig. 15. In Fig. 14, the CP symmetry relating $\chi_j = \chi_{2L-1-j}$ is used to effectively double the number of shots, resulting in statistical error bars that are smaller by a factor of $\sqrt{2}$.

In an effort to explore the limitations of the quantum computer, the three-step SC-ADAPT-VQE state preparation circuits for $L = 30$ and $L = 50$ were implemented on `ibm_brisbane` and `ibm_cusco`, respectively. The structure of the ansatz wave function and corresponding variational parameters can be found in Table XII. The local chiral condensate and charge-charge correlators obtained from 80 ($L = 30$) and 40 ($L = 50$) twirled instances, each with 8×10^3 shots, are shown in Figs. 16 and 17. Despite the factor of 3 increase in the number of CNOT gates relative to two layers (1254 versus 468 for $L = 30$, and 2134 versus 788 for $L = 50$), the results are consistent with those obtained from the Qiskit MPS circuit simulator. Note that

TABLE XII. Extrapolation of the variational parameters corresponding to two and three steps of SC-ADAPT-VQE with $m = 0.5$ and $g = 0.3$. These parameters were used in the circuits run on `ibm_brisbane` ($L \leq 40$) and `ibm_cusco` ($L = 50$).

L	Two steps		Three steps		
	$\hat{O}_{mh}^V(1)$	$\hat{O}_{mh}^V(3)$	$\hat{O}_{mh}^V(1)$	$\hat{O}_{mh}^V(3)$	$\hat{O}_{mh}^V(5)$
	θ_i				
14	0.30699	-0.04033			
20	0.30638	-0.03994			
30	0.30610	-0.03978	0.30630	-0.04092	0.00671
40	0.30605	-0.03975			
50	0.30604	-0.03975	0.30624	-0.04089	0.00670

qubit 0 and 2 have decohered for both volumes, and in principle could be removed from volume-averaged quantities, such as the chiral condensate.

By our sending the circuits with the Sampler primitive, several error-mitigation techniques are applied during runtime, as mentioned in Sec. VB. Specifically, the readout mitigation technique used (for $L \leq 40$) is M3 [147]. This method is based on correcting only the subspace of bit strings observed in the noisy raw counts from the machine (which usually include the ideal ones plus those with short Hamming distance, introduced by the noise in the measurement), and using Krylov subspace methods to avoid having to compute (and store) the full assignment matrix.

Unlike other studies that used 100 or more superconducting qubits [155–157], which used zero-noise extrapolation (ZNE) [178–180] in conjunction with probabilistic error correction (PEC) [179,181] to remove incoherent errors, we use ODR, as explained in Appendix E. Both methods require first transforming coherent errors into incoherent errors, which is done via Pauli twirling. However, the overhead in sampling using ZNE and PCE, compared with ODR, is substantial. For ZNE, one has to add two-qubit gates to increase the noise level, and then perform an extrapolation to estimate the noiseless result. In the minimal case, this leads to running only another circuit, like in ODR, but with a circuit depth that is 3 times as large as the original circuit (e.g., replacing each CNOT gate with three CNOT gates). However, this leads to a large uncertainty in the functional form of the extrapolation, and ideally the circuit is run with multiple noise levels to have multiple points from which to extrapolate. For PEC, the overhead is even larger, as it involves learning the noise model of the chip, by running multiple random circuits with different depths (see Ref. [181]). For ODR,

TABLE XIII. Two-Pauli-gate set (G_2, G_2') used to generate the twirled ECR gates, $G_2' \cdot \text{ECR} \cdot G_2 = \text{ECR}$.

$(\hat{I} \otimes \hat{I}, \hat{I} \otimes \hat{I})$	$(\hat{I} \otimes \hat{X}, \hat{I} \otimes \hat{X})$	$(\hat{I} \otimes \hat{Y}, \hat{Z} \otimes \hat{Z})$	$(\hat{I} \otimes \hat{Z}, \hat{Z} \otimes \hat{Y})$	$(\hat{X} \otimes \hat{I}, \hat{Y} \otimes \hat{X})$	$(\hat{X} \otimes \hat{X}, \hat{Y} \otimes \hat{I})$	$(\hat{X} \otimes \hat{Y}, \hat{X} \otimes \hat{Y})$	$(\hat{X} \otimes \hat{Z}, \hat{X} \otimes \hat{Z})$
$(\hat{Y} \otimes \hat{I}, \hat{X} \otimes \hat{X})$	$(\hat{Y} \otimes \hat{X}, \hat{X} \otimes \hat{I})$	$(\hat{Y} \otimes \hat{Y}, \hat{Y} \otimes \hat{Y})$	$(\hat{Y} \otimes \hat{Z}, \hat{Y} \otimes \hat{Z})$	$(\hat{Z} \otimes \hat{I}, \hat{Z} \otimes \hat{I})$	$(\hat{Z} \otimes \hat{X}, \hat{Z} \otimes \hat{X})$	$(\hat{Z} \otimes \hat{Y}, \hat{I} \otimes \hat{Z})$	$(\hat{Z} \otimes \hat{Z}, \hat{I} \otimes \hat{Y})$

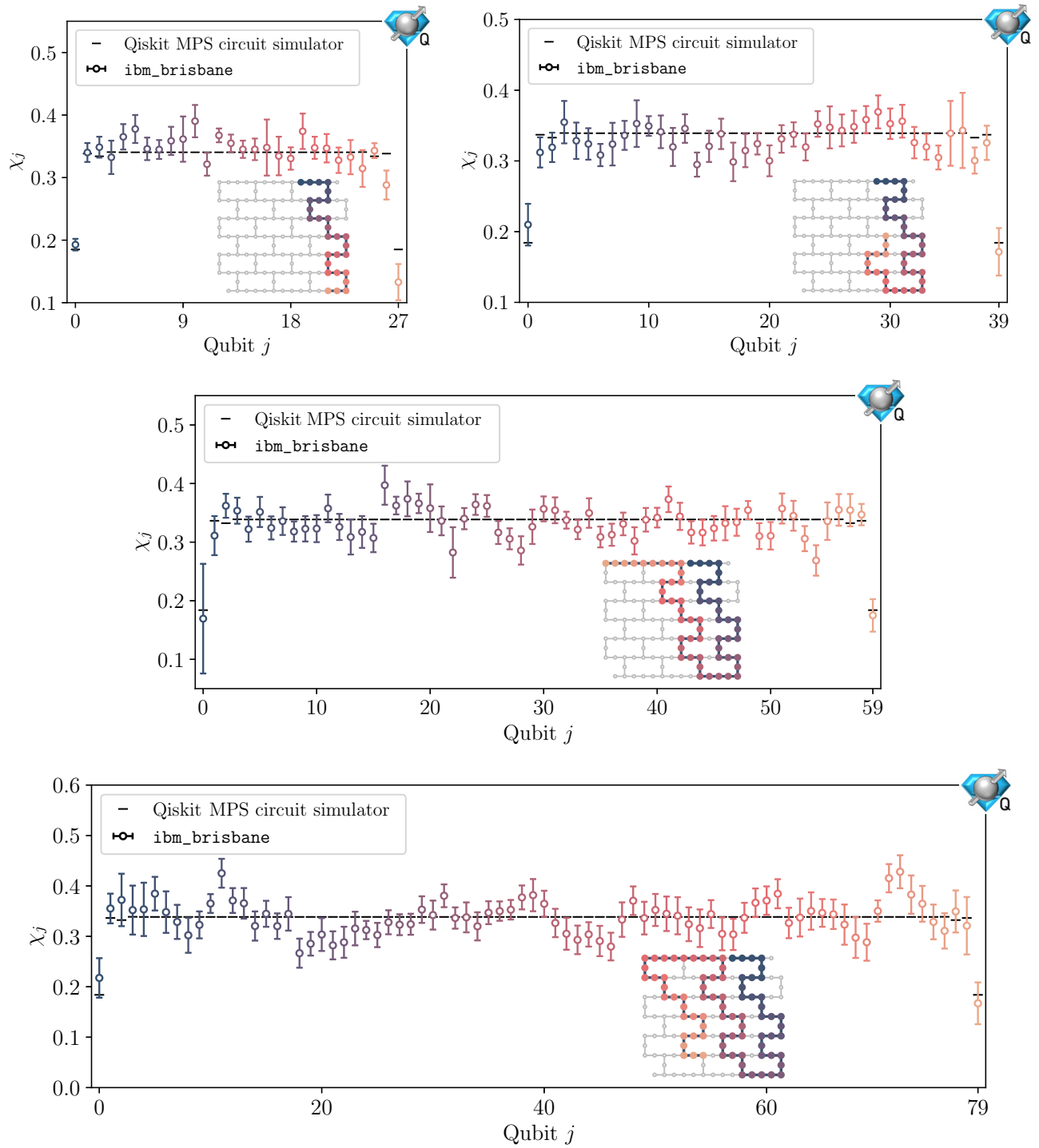


FIG. 13. Expectation values of χ_j for $L = 14, 20, 30,$ and 40 (from top to bottom) obtained from simulations using `ibm_brisbane`. They are compared with the expected results obtained with use of Qiskit’s MPS circuit simulator (black dashes). Averaging χ_j over all of the qubits provides the chiral condensates presented in Table IV. The layouts of the qubits used on the chip are shown in the insets.

as explained in Appendix E, only the same “physics” circuits are run, but with all rotations set to zero, meaning the sampling overhead is only doubled.

To generate the different twirled circuits, the set of two-qubit Pauli gates G_2 and G'_2 that leave the (noisy) two-qubit gate invariant (up to a global phase) must be identified. For

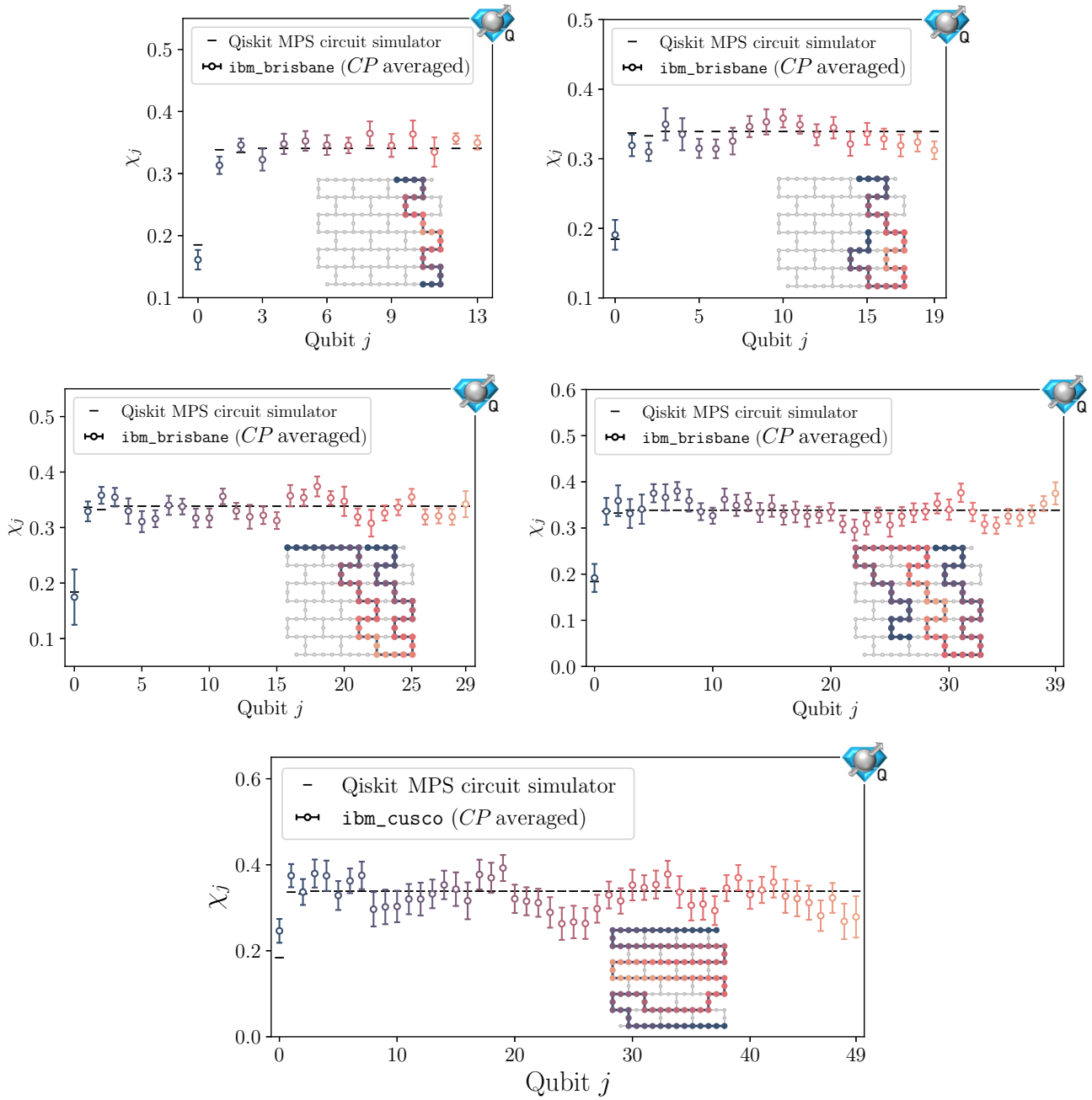


FIG. 14. Expectation values of CP -averaged χ_j for $L = 14, 20, 30, 40,$ and 50 (from top to bottom) obtained from simulations using `ibm_brisbane` and `ibm_cusco`. They are compared with the expected results obtained with use of Qiskit’s MPS circuit simulator (black dashes). The layouts of the qubits used on the chip are shown in the insets (with same-colored qubits being averaged).

the quantum processors used in this work, the native two-qubit gate is the echoed cross-resonance (ECR) gate, which

is equivalent to the CNOT gate via single-qubit rotations. Explicitly,

$$ECR = \frac{1}{\sqrt{2}}(\hat{X} \otimes \hat{I} - \hat{Y} \otimes \hat{X}),$$

ECR

=

(G1)

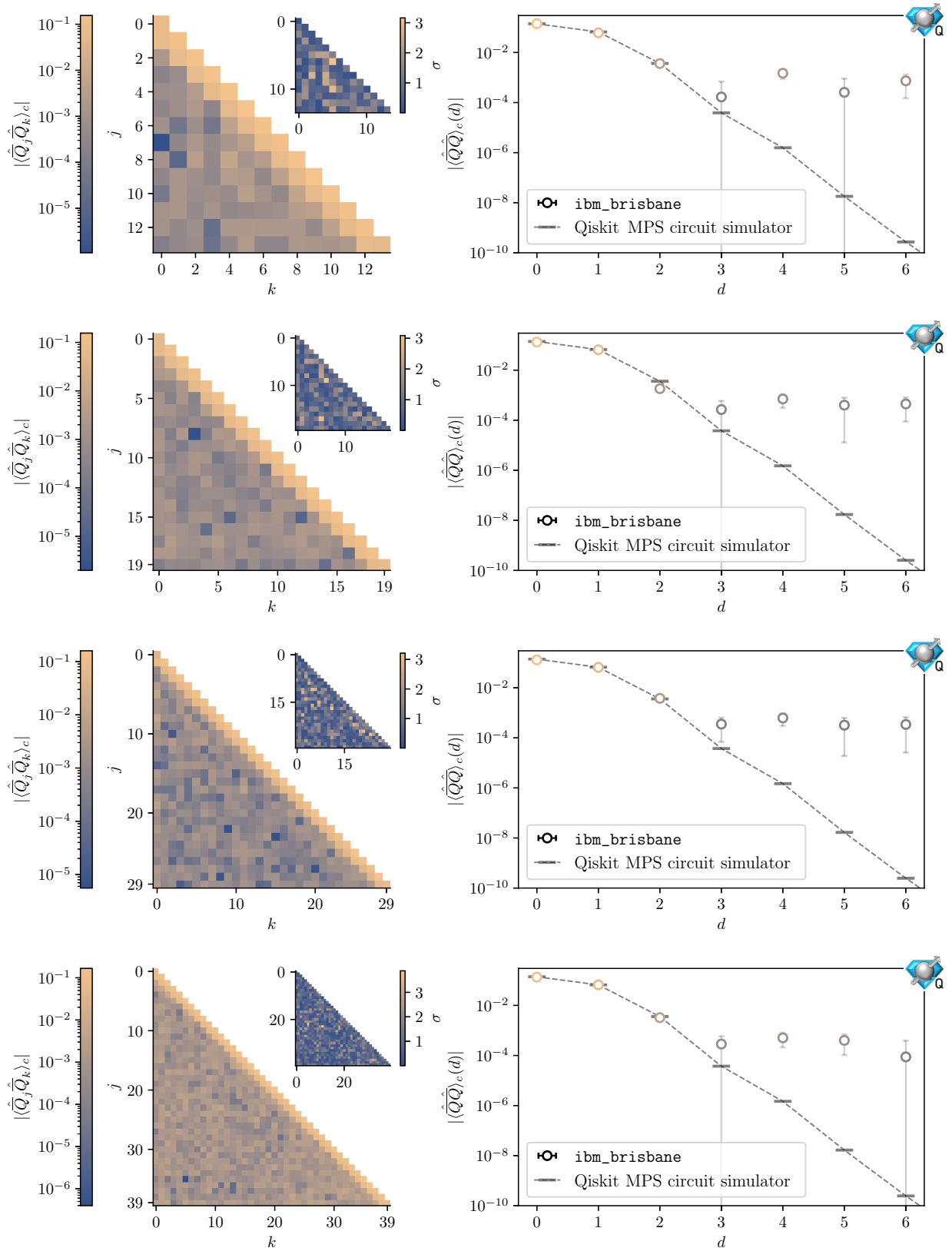


FIG. 15. Connected contribution to the spatial charge-charge correlation functions, $\langle \hat{Q}_j \hat{Q}_k \rangle_c$ (left) and averaged correlation functions as a function of distance d , $\langle \hat{Q} \hat{Q} \rangle_c(d)$ (right), with the points following the same color map as in the left main panel (error bars show 1σ standard deviations). Results obtained from `ibm_brisbane` are shown for $L = 14, 20, 30$, and 40 (from top to bottom).

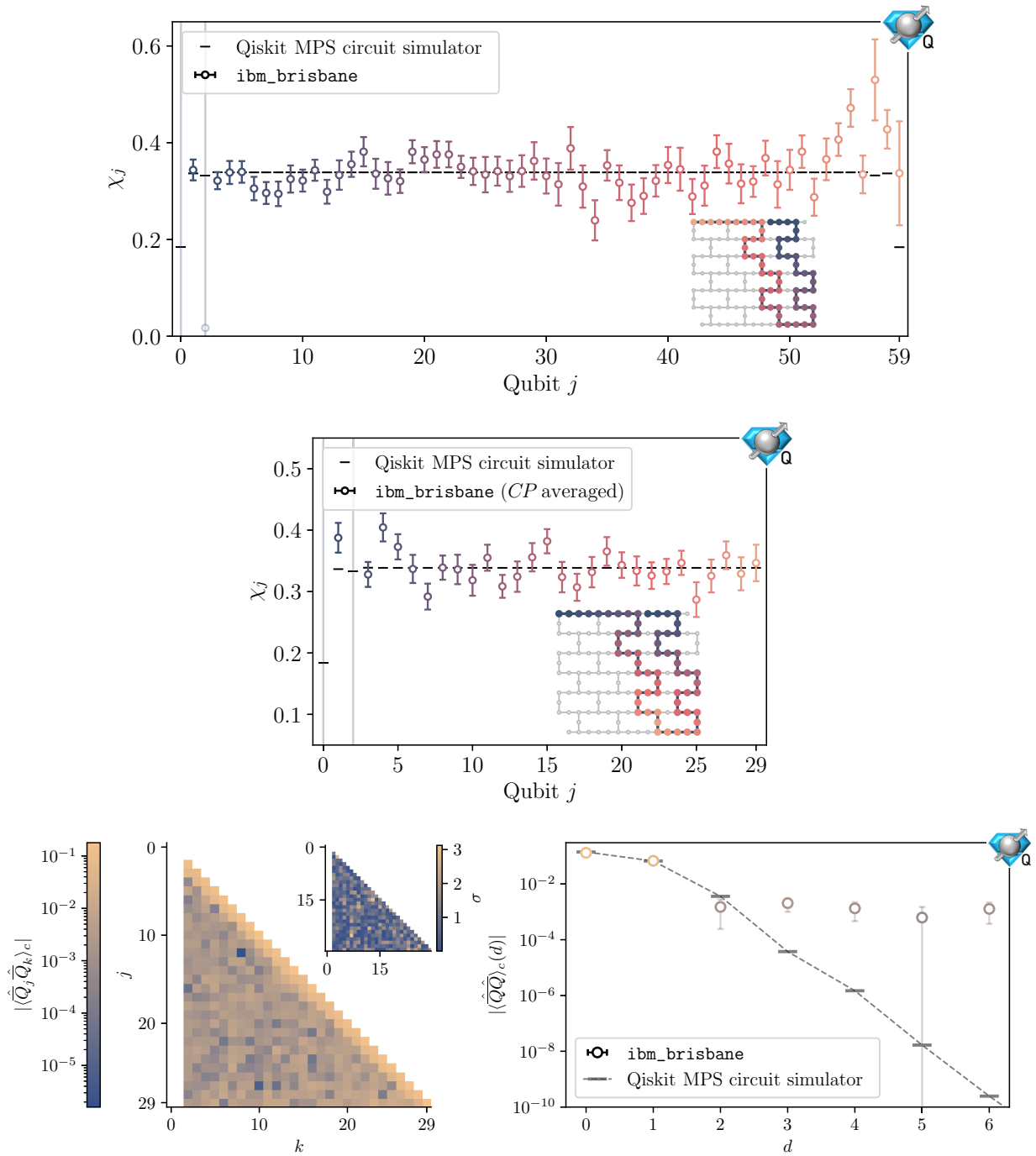


FIG. 16. Results for the $L = 30$ system obtained with use of three steps of SC-ADAPT-VQE, obtained from simulations using `ibm_brisbane` with 80 twirled instances. The top panel shows χ_j , the middle panel shows the CP -averaged χ_j , and the bottom panels show the connected contribution to the spatial charge-charge correlation functions, $\langle \hat{Q}_j \hat{Q}_k \rangle_c$ (the first two spatial sites are not shown due to the errors on qubits 0 and 2), and the averaged correlation functions as a function of distance d , $\langle \hat{Q} \hat{Q} \rangle_c(d)$, with the points following the same color map as in the left main panel (error bars show 1σ standard deviations).

Using the functions from the package `qiskit_research` [182], together with the two-Pauli-gate set shown in Table XIII, we generated a total of 40 (150) twirled circuits for both mitigation and physics for $L \leq 40$ ($L = 50$), each with 8×10^3 shots.

From Fig. 7, the effects of each error-mitigation method can be seen. The first set of results shown are semiraw, obtained directly from the quantum computer. They are not raw since DD is integrated into the circuits that are run on the machine (REM is also included for $L \leq 40$). To check

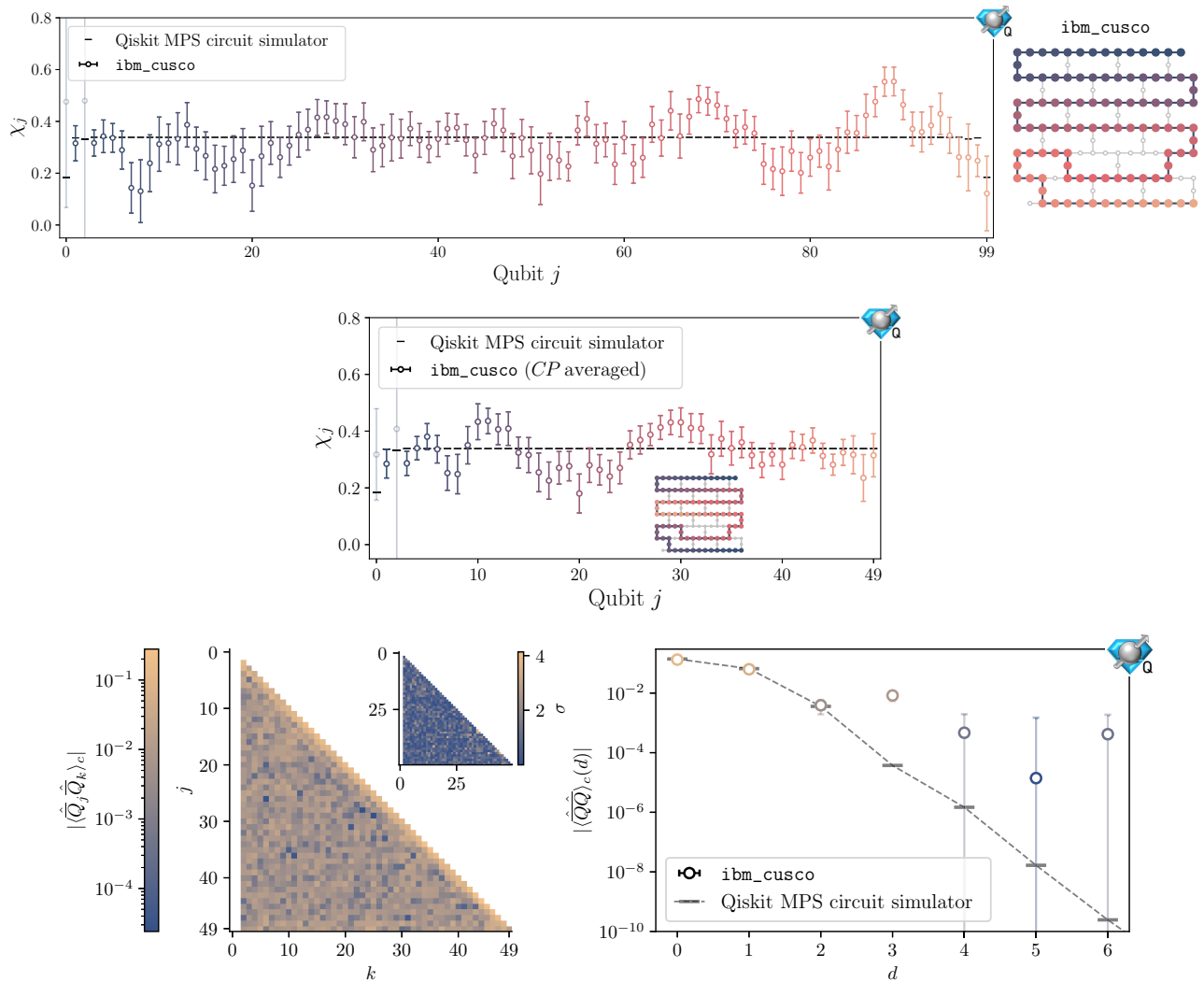


FIG. 17. Results for the $L = 50$ system obtained with use of three steps of SC-ADAPT-VQE, obtained from simulations using `ibm_cusco` with 40 twirled instances. The top panel shows χ_j , the middle panel shows the CP -averaged χ_j , and the bottom panels show the connected contribution to the spatial charge-charge correlation functions, $\langle \hat{Q}_j \hat{Q}_k \rangle_c$ (the first two spatial sites are not shown due to the errors on qubits 0 and 2), and the averaged correlation functions as a function of distance d , $\langle \hat{Q}_j \hat{Q}_k \rangle_c(d)$, with the points following the same color map as in the left main panel (error bars show 1σ standard deviations).

the effect that DD has, several runs were performed without it, and a degradation of the signal was visible when qubits were idle for long periods (the effects of not using DD were more evident when the deeper three-step circuit was run). Regarding REM, while the final fully mitigated results for $L = 50$ (no REM applied) and $L \leq 40$ (REM applied) systems are similar in quality, a larger statistical sample for $L = 50$ was required to achieve an equivalent level of precision (2.4×10^6 shots versus 6.4×10^5 shots). The second set shows the effects of applying PT (the results for no Pauli twirling corresponded to one twirled instance). It is seen that all the coherent noise on the different qubits has been transformed into uniform incoherent noise. The last set shown is after ODR has been used to remove the incoherent noise.

- [1] S. Weinberg, A model of leptons, *Phys. Rev. Lett.* **19**, 1264 (1967).
- [2] S. Glashow, Partial symmetries of weak interactions, *Nucl. Phys.* **22**, 579 (1961).
- [3] A. Salam, Weak and electromagnetic interactions, *Conf. Proc. C* **680519**, 367 (1968).
- [4] H. Politzer, Reliable perturbative results for strong interactions?, *Phys. Rev. Lett.* **30**, 1346 (1973).
- [5] D. J. Gross and F. Wilczek, Ultraviolet behavior of non-abelian gauge theories, *Phys. Rev. Lett.* **30**, 1343 (1973).
- [6] P. W. Higgs, Broken symmetries and the masses of gauge bosons, *Phys. Rev. Lett.* **13**, 508 (1964).
- [7] M. C. Bañuls, *et al.*, Simulating lattice gauge theories within quantum technologies, *Eur. Phys. J. D* **74**, 165 (2020).

- [8] W. Guan, G. Perdue, A. Pesah, M. Schuld, K. Terashi, S. Vallecorsa, and J.-R. Vlimant, Quantum machine learning in high energy physics, *Mach. Learn.: Sci. Technol.* **2**, 011003 (2021).
- [9] N. Klco, A. Roggero, and M. J. Savage, Standard model physics and the digital quantum revolution: thoughts about the interface, *Rept. Prog. Phys.* **85**, 064301 (2022).
- [10] A. Delgado, *et al.*, in *Snowmass 2021*, arXiv:2203.08805.
- [11] C. W. Bauer, *et al.*, Quantum simulation for high-energy physics, *PRX Quantum* **4**, 027001 (2023).
- [12] T. S. Humble, G. N. Perdue, and M. J. Savage, Snowmass computational frontier: Topical group report on quantum computing, arXiv:2209.06786.
- [13] D. Beck, *et al.*, Quantum information science and technology for nuclear physics. Input into U.S. long-range planning, arXiv:2303.00113.
- [14] C. W. Bauer, Z. Davoudi, N. Klco, and M. J. Savage, Quantum simulation of fundamental particles and forces, *Nat. Rev. Phys.* **5**, 420 (2023).
- [15] A. Di Meglio, *et al.*, Quantum computing for high-energy physics: State of the art and challenges. Summary of the QC4HEP Working Group, arXiv:2307.03236.
- [16] S. Lloyd, Universal quantum simulators, *Science* **273**, 1073 (1996).
- [17] J. Kempe, A. Kitaev, and O. Regev, in *FSTTCS 2004: Foundations of Software Technology and Theoretical Computer Science*, edited by K. Lodaya and M. Mahajan (Springer Berlin Heidelberg, Berlin, Heidelberg, 2005), p. 372.
- [18] Note that adiabatic state preparation resides within the bounded-error quantum polynomial time complexity class when there is a path through parameter space in which the system remains gapped [20,21]. However, even in gapped systems, the gate count required for adiabatic preparation can be daunting; see, e.g., Ref. [22], where adiabatic preparation of the Schwinger model vacuum on 16 qubits was estimated to require 2.7×10^5 two-qubit gates.
- [19] Systems of importance to nuclear physics and high-energy physics are constrained by a number of local, exact global, and approximately global symmetries, some of which are emergent from the mechanisms of confinement and spontaneous symmetry breaking.
- [20] E. Farhi, J. Goldstone, S. Gutmann, and M. Sipser, Quantum computation by adiabatic evolution, arXiv:quant-ph/0001106.
- [21] W. van Dam, M. Mosca, and U. Vazirani, in *Proceedings 42nd IEEE Symposium on Foundations of Computer Science (IEEE, 2001)*.
- [22] B. Chakraborty, M. Honda, T. Izubuchi, Y. Kikuchi, and A. Tomiya, Classically emulated digital quantum simulation of the Schwinger model with a topological term via adiabatic state preparation, *Phys. Rev. D* **105**, 094503 (2022).
- [23] J. S. Schwinger, Gauge invariance and mass. II, *Phys. Rev.* **128**, 2425 (1962).
- [24] E. A. Martinez, C. A. Muschik, P. Schindler, D. Nigg, A. Erhard, M. Heyl, P. Hauke, M. Dalmonte, T. Monz, P. Zoller, and R. Blatt, Real-time dynamics of lattice gauge theories with a few-qubit quantum computer, *Nature* **534**, 516 (2016).
- [25] C. Kokail, C. Maier, R. van Bijnen, T. Brydges, M. K. Joshi, P. Jurcevic, C. A. Muschik, P. Silvi, R. Blatt, C. F. Roos, and P. Zoller, Self-verifying variational quantum simulation of lattice models, *Nature* **569**, 355 (2019).
- [26] N. H. Nguyen, M. C. Tran, Y. Zhu, A. M. Green, C. H. Alderete, Z. Davoudi, and N. M. Linke, Digital quantum simulation of the Schwinger model and symmetry protection with trapped ions, *PRX Quantum* **3**, 020324 (2022).
- [27] N. Mueller, J. A. Carolan, A. Connelly, Z. Davoudi, E. F. Dumitrescu, and K. Yeter-Aydeniz, Quantum computation of dynamical quantum phase transitions and entanglement tomography in a lattice gauge theory, arXiv:2210.03089.
- [28] N. Klco, E. F. Dumitrescu, A. J. McCaskey, T. D. Morris, R. C. Pooser, M. Sanz, E. Solano, P. Lougovski, and M. J. Savage, Quantum-classical computation of Schwinger model dynamics using quantum computers, *Phys. Rev. A* **98**, 032331 (2018).
- [29] G. Mazzola, S. V. Mathis, G. Mazzola, and I. Tavernelli, Gauge-invariant quantum circuits for $U(1)$ and Yang-Mills lattice gauge theories, *Phys. Rev. Res.* **3**, 043209 (2021).
- [30] W. A. de Jong, K. Lee, J. Mulligan, M. Płoskoń, F. Ringer, and X. Yao, Quantum simulation of nonequilibrium dynamics and thermalization in the Schwinger model, *Phys. Rev. D* **106**, 054508 (2022).
- [31] W. Gong, G. Parida, Z. Tu, and R. Venugopalan, Measurement of Bell-type inequalities and quantum entanglement from Λ -hyperon spin correlations at high energy colliders, *Phys. Rev. D* **106**, L031501 (2022).
- [32] J. Mildenerger, W. Mruczkiewicz, J. C. Halimeh, Z. Jiang, and P. Hauke, Probing confinement in a \mathbb{Z}_2 lattice gauge theory on a quantum computer, arXiv:2203.08905.
- [33] C. Charles, E. J. Gustafson, E. Hardt, F. Herren, N. Hogan, H. Lamm, S. Starecheski, R. S. Van de Water, and M. L. Wagman, Simulating \mathbb{Z}_2 lattice gauge theory on a quantum computer, arXiv:2305.02361.
- [34] D. Pomarico, L. Cosmai, P. Facchi, C. Lupo, S. Pascazio, and F. V. Pepe, Dynamical quantum phase transitions of the Schwinger model: Real-time dynamics on IBM Quantum, *Entropy* **25**, 608 (2023).
- [35] H.-H. Lu, N. Klco, J. M. Lukens, T. D. Morris, A. Bansal, A. Ekström, G. Hagen, T. Papenbrock, A. M. Weiner, M. J. Savage, and P. Lougovski, Simulations of subatomic many-body physics on a quantum frequency processor, *Phys. Rev. A* **100**, 012320 (2019).
- [36] F. M. Surace, P. P. Mazza, G. Giudici, A. Leroose, A. Gambassi, and M. Dalmonte, Lattice gauge theories and string dynamics in Rydberg atom quantum simulators, *Phys. Rev. X* **10**, 021041 (2020).
- [37] A. Mil, T. V. Zache, A. Hegde, A. Xia, R. P. Bhatt, M. K. Oberthaler, P. Hauke, J. Berges, and F. Jendrzejewski, A scalable realization of local $U(1)$ gauge invariance in cold atomic mixtures, *Science* **367**, 1128 (2020).
- [38] B. Yang, H. Sun, R. Ott, H.-Y. Wang, T. V. Zache, J. C. Halimeh, Z.-S. Yuan, P. Hauke, and J.-W. Pan, Observation of gauge invariance in a 71-site Bose-Hubbard quantum simulator, *Nature* **587**, 392 (2020).
- [39] Z.-Y. Zhou, G.-X. Su, J. C. Halimeh, R. Ott, H. Sun, P. Hauke, B. Yang, Z.-S. Yuan, J. Berges, and J.-W. Pan,

- Thermalization dynamics of a gauge theory on a quantum simulator, *Science* **377**, 311 (2022).
- [40] G.-X. Su, H. Sun, A. Hudomal, J.-Y. Desaulles, Z.-Y. Zhou, B. Yang, J. C. Halimeh, Z.-S. Yuan, Z. Papić, and J.-W. Pan, Observation of many-body scarring in a Bose-Hubbard quantum simulator, *Phys. Rev. Res.* **5**, 023010 (2023).
- [41] W.-Y. Zhang, Y. Liu, Y. Cheng, M.-G. He, H.-Y. Wang, T.-Y. Wang, Z.-H. Zhu, G.-X. Su, Z.-Y. Zhou, Y.-G. Zheng, H. Sun, B. Yang, P. Hauke, W. Zheng, J. C. Halimeh, Z.-S. Yuan, and J.-W. Pan, Observation of microscopic confinement dynamics by a tunable topological θ -angle, [arXiv:2306.11794](https://arxiv.org/abs/2306.11794).
- [42] H. Riechert, J. C. Halimeh, V. Kasper, L. Bretheau, E. Zohar, P. Hauke, and F. Jendrzejewski, Engineering a U(1) lattice gauge theory in classical electric circuits, *Phys. Rev. B* **105**, 205141 (2022).
- [43] D. Banerjee, M. Dalmonte, M. Muller, E. Rico, P. Stebler, U. J. Wiese, and P. Zoller, Atomic quantum simulation of dynamical gauge fields coupled to fermionic matter: from string breaking to evolution after a quench, *Phys. Rev. Lett.* **109**, 175302 (2012).
- [44] D. Marcos, P. Rabl, E. Rico, and P. Zoller, Superconducting circuits for quantum simulation of dynamical gauge fields, *Phys. Rev. Lett.* **111**, 110504 (2013).
- [45] D. Yang, G. S. Giri, M. Johanning, C. Wunderlich, P. Zoller, and P. Hauke, Analog quantum simulation of (1+1)-dimensional lattice QED with trapped ions, *Phys. Rev. A* **94**, 052321 (2016).
- [46] C. Muschik, M. Heyl, E. Martinez, T. Monz, P. Schindler, B. Vogell, M. Dalmonte, P. Hauke, R. Blatt, and P. Zoller, U(1) Wilson lattice gauge theories in digital quantum simulators, *New J. Phys.* **19**, 103020 (2017).
- [47] Z. Davoudi, M. Hafezi, C. Monroe, G. Pagano, A. Seif, and A. Shaw, Towards analog quantum simulations of lattice gauge theories with trapped ions, *Phys. Rev. Res.* **2**, 023015 (2020).
- [48] D. Luo, J. Shen, M. Highman, B. K. Clark, B. DeMarco, A. X. El-Khadra, and B. Gadway, Framework for simulating gauge theories with dipolar spin systems, *Phys. Rev. A* **102**, 032617 (2020).
- [49] R. R. Ferguson, L. Dellantonio, K. Jansen, A. A. Balushi, W. Dür, and C. A. Muschik, Measurement-based variational quantum eigensolver, *Phys. Rev. Lett.* **126**, 220501 (2021).
- [50] Z. Davoudi, N. M. Linke, and G. Pagano, Toward simulating quantum field theories with controlled phonon-ion dynamics: A hybrid analog-digital approach, *Phys. Rev. Res.* **3**, 043072 (2021).
- [51] A. Yamamoto, Quantum variational approach to lattice gauge theory at nonzero density, *Phys. Rev. D* **104**, 014506 (2021).
- [52] M. Honda, E. Itou, Y. Kikuchi, L. Nagano, and T. Okuda, Classically emulated digital quantum simulation for screening and confinement in the Schwinger model with a topological term, *Phys. Rev. D* **105**, 014504 (2022).
- [53] E. R. Bennowitz, F. Hopfmueller, B. Kulchytsky, J. Carrasquilla, and P. Ronagh, Neural error mitigation of near-term quantum simulations, *Nature Mach. Intell.* **4**, 618 (2022).
- [54] B. Andrade, Z. Davoudi, T. Graß, M. Hafezi, G. Pagano, and A. Seif, Engineering an effective three-spin Hamiltonian in trapped-ion systems for applications in quantum simulation, *Quantum Sci. Technol.* **7**, 034001 (2022).
- [55] M. Honda, E. Itou, Y. Kikuchi, and Y. Tanizaki, Negative string tension of a higher-charge Schwinger model via digital quantum simulation, *PTEP* **2022**, 033B01 (2022).
- [56] J. C. Halimeh, I. P. McCulloch, B. Yang, and P. Hauke, Tuning the topological θ -angle in cold-atom quantum simulators of gauge theories, *PRX Quantum* **3**, 040316 (2022).
- [57] X.-D. Xie, X. Guo, H. Xing, Z.-Y. Xue, D.-B. Zhang, and S.-L. Zhu (QuNu), Variational thermal quantum simulation of the lattice Schwinger model, *Phys. Rev. D* **106**, 054509 (2022).
- [58] Z. Davoudi, N. Mueller, and C. Powers, Toward quantum computing phase diagrams of gauge theories with thermal pure quantum states, [arXiv:2208.13112](https://arxiv.org/abs/2208.13112).
- [59] L. Nagano, A. Bapat, and C. W. Bauer, Quench dynamics of the Schwinger model via variational quantum algorithms, [arXiv:2302.10933](https://arxiv.org/abs/2302.10933).
- [60] P. P. Popov, M. Meth, M. Lewenstein, P. Hauke, M. Ringbauer, E. Zohar, and V. Kasper, Variational quantum simulation of U(1) lattice gauge theories with qudit systems, [arXiv:2307.15173](https://arxiv.org/abs/2307.15173).
- [61] L. Nagano, A. Miessen, T. Onodera, I. Tavernelli, F. Tacchino, and K. Terashi, Quantum data learning for quantum simulations in high-energy physics, [arXiv:2306.17214](https://arxiv.org/abs/2306.17214).
- [62] P. Hauke, D. Marcos, M. Dalmonte, and P. Zoller, Quantum simulation of a lattice Schwinger model in a chain of trapped ions, *Phys. Rev. X* **3**, 041018 (2013).
- [63] V. Kasper, F. Hebenstreit, F. Jendrzejewski, M. K. Oberthaler, and J. Berges, Implementing quantum electrodynamics with ultracold atomic systems, *New J. Phys.* **19**, 023030 (2017).
- [64] S. Notarnicola, M. Collura, and S. Montangero, Real-time-dynamics quantum simulation of (1+1)-dimensional lattice QED with Rydberg atoms, *Phys. Rev. Res.* **2**, 013288 (2020).
- [65] M. C. Tran, Y. Su, D. Carney, and J. M. Taylor, Faster digital quantum simulation by symmetry protection, *PRX Quantum* **2**, 010323 (2021).
- [66] J. Shen, D. Luo, C. Huang, B. K. Clark, A. X. El-Khadra, B. Gadway, and P. Draper, Simulating quantum mechanics with a θ -term and an 't Hooft anomaly on a synthetic dimension, *Phys. Rev. D* **105**, 074505 (2022).
- [67] R. B. Jensen, S. P. Pedersen, and N. T. Zinner, Dynamical quantum phase transitions in a noisy lattice gauge theory, *Phys. Rev. B* **105**, 224309 (2022).
- [68] A. Florio, D. Frenklakh, K. Ikeda, D. Kharzeev, V. Korepin, S. Shi, and K. Yu, Real-time nonperturbative dynamics of jet production in Schwinger model: Quantum entanglement and vacuum modification, *Phys. Rev. Lett.* **131**, 021902 (2023).
- [69] K. Ikeda, D. E. Kharzeev, R. Meyer, and S. Shi, Detecting the critical point through entanglement in Schwinger model, [arXiv:2305.00996](https://arxiv.org/abs/2305.00996).
- [70] T. Byrnes, P. Sriganesh, R. J. Bursill, and C. J. Hamer, Density matrix renormalization group approach to the

- massive Schwinger model, *Phys. Rev. D* **66**, 013002 (2002).
- [71] M. C. Bañuls, K. Cichy, K. Jansen, and J. I. Cirac, The mass spectrum of the Schwinger model with matrix product states, *JHEP* **11**, 158 (2013).
- [72] E. Rico, T. Pichler, M. Dalmonte, P. Zoller, and S. Montangero, Tensor networks for lattice gauge theories and atomic quantum simulation, *Phys. Rev. Lett.* **112**, 201601 (2014).
- [73] B. Buyens, J. Haegeman, K. Van Acoleyen, H. Verschelde, and F. Verstraete, Matrix product states for gauge field theories, *Phys. Rev. Lett.* **113**, 091601 (2014).
- [74] S. Kühn, J. I. Cirac, and M.-C. Bañuls, Quantum simulation of the Schwinger model: A study of feasibility, *Phys. Rev. A* **90**, 042305 (2014).
- [75] M. C. Bañuls, K. Cichy, J. I. Cirac, K. Jansen, and H. Saito, Thermal evolution of the Schwinger model with matrix product operators, *Phys. Rev. D* **92**, 034519 (2015).
- [76] T. Pichler, M. Dalmonte, E. Rico, P. Zoller, and S. Montangero, Real-time dynamics in U(1) lattice gauge theories with tensor networks, *Phys. Rev. X* **6**, 011023 (2016).
- [77] B. Buyens, J. Haegeman, H. Verschelde, F. Verstraete, and K. Van Acoleyen, Confinement and string breaking for QED₂ in the Hamiltonian picture, *Phys. Rev. X* **6**, 041040 (2016).
- [78] M. C. Bañuls, K. Cichy, K. Jansen, and H. Saito, Chiral condensate in the Schwinger model with matrix product operators, *Phys. Rev. D* **93**, 094512 (2016).
- [79] B. Buyens, F. Verstraete, and K. Van Acoleyen, Hamiltonian simulation of the Schwinger model at finite temperature, *Phys. Rev. D* **94**, 085018 (2016).
- [80] B. Buyens, J. Haegeman, F. Hebenstreit, F. Verstraete, and K. Van Acoleyen, Real-time simulation of the Schwinger effect with matrix product states, *Phys. Rev. D* **96**, 114501 (2017).
- [81] K. Zapp and R. Orus, Tensor network simulation of QED on infinite lattices: Learning from (1 + 1) d, and prospects for (2 + 1) d, *Phys. Rev. D* **95**, 114508 (2017).
- [82] E. Ercolessi, P. Facchi, G. Magnifico, S. Pascazio, and F. V. Pepe, Phase transitions in Z_n gauge models: Towards quantum simulations of the Schwinger-Weyl QED, *Phys. Rev. D* **98**, 074503 (2018).
- [83] P. Sala, T. Shi, S. Kühn, M. C. Bañuls, E. Demler, and J. I. Cirac, Variational study of U(1) and SU(2) lattice gauge theories with Gaussian states in 1 + 1 dimensions, *Phys. Rev. D* **98**, 034505 (2018).
- [84] L. Funcke, K. Jansen, and S. Kühn, Topological vacuum structure of the Schwinger model with matrix product states, *Phys. Rev. D* **101**, 054507 (2020).
- [85] G. Magnifico, M. Dalmonte, P. Facchi, S. Pascazio, F. V. Pepe, and E. Ercolessi, Real time dynamics and confinement in the Z_n Schwinger-Weyl lattice model for 1+1 QED, *Quantum* **4**, 281 (2020).
- [86] N. Butt, S. Catterall, Y. Meurice, R. Sakai, and J. Unmuth-Yockey, Tensor network formulation of the massless Schwinger model with staggered fermions, *Phys. Rev. D* **101**, 094509 (2020).
- [87] M. Rigobello, S. Notarnicola, G. Magnifico, and S. Montangero, Entanglement generation in (1+1)D QED scattering processes, *Phys. Rev. D* **104**, 114501 (2021).
- [88] T. Okuda, Schwinger model on an interval: Analytic results and DMRG, *Phys. Rev. D* **107**, 054506 (2023).
- [89] M. Honda, E. Itou, and Y. Tanizaki, DMRG study of the higher-charge Schwinger model and its 't Hooft anomaly, *JHEP* **11**, 141 (2022).
- [90] J.-Y. Desaulles, G.-X. Su, I. P. McCulloch, B. Yang, Z. Papić, and J. C. Halimeh, Ergodicity breaking under confinement in cold-atom quantum simulators, [arXiv:2301.07717](https://arxiv.org/abs/2301.07717).
- [91] T. Angelides, L. Funcke, K. Jansen, and S. Kühn, Computing the mass shift of Wilson and staggered fermions in the lattice Schwinger model with matrix product states, *Phys. Rev. D* **108**, 014516 (2023).
- [92] R. Belyansky, S. Whitsitt, N. Mueller, A. Fahimniya, E. R. Bennewitz, Z. Davoudi, and A. V. Gorshkov, High-energy collision of quarks and hadrons in the Schwinger model: From tensor networks to circuit QED, [arXiv:2307.02522](https://arxiv.org/abs/2307.02522).
- [93] M. C. Bañuls and K. Cichy, Review on novel methods for lattice gauge theories, *Rep. Prog. Phys.* **83**, 024401 (2020).
- [94] Y. Y. Atas, J. Zhang, R. Lewis, A. Jahanpour, J. F. Haase, and C. A. Muschik, SU(2) hadrons on a quantum computer via a variational approach, *Nat. Commun.* **12**, 6499 (2021).
- [95] Y. Y. Atas, J. F. Haase, J. Zhang, V. Wei, S. M. L. Pfaendler, R. Lewis, and C. A. Muschik, Simulating one-dimensional quantum chromodynamics on a quantum computer: Real-time evolutions of tetra- and pentaquarks, [arXiv:2207.03473](https://arxiv.org/abs/2207.03473).
- [96] R. C. Farrell, I. A. Chernyshev, S. J. M. Powell, N. A. Zemlevskiy, M. Illa, and M. J. Savage, Preparations for quantum simulations of quantum chromodynamics in 1+1 dimensions. II. Single-baryon β -decay in real time, *Phys. Rev. D* **107**, 054513 (2023).
- [97] R. C. Farrell, I. A. Chernyshev, S. J. M. Powell, N. A. Zemlevskiy, M. Illa, and M. J. Savage, Preparations for quantum simulations of quantum chromodynamics in 1+1 dimensions. I. Axial gauge, *Phys. Rev. D* **107**, 054512 (2023).
- [98] A. N. Ciavarella, Quantum simulation of lattice QCD with improved Hamiltonians, [arXiv:2307.05593](https://arxiv.org/abs/2307.05593).
- [99] S. Kühn, E. Zohar, J. I. Cirac, and M. C. Bañuls, Non-Abelian string breaking phenomena with matrix product states, *JHEP* **07**, 130 (2015).
- [100] N. Klco, J. R. Stryker, and M. J. Savage, SU(2) non-Abelian gauge field theory in one dimension on digital quantum computers, *Phys. Rev. D* **101**, 074512 (2020).
- [101] A. Ciavarella, N. Klco, and M. J. Savage, Trailhead for quantum simulation of SU(3) Yang-Mills lattice gauge theory in the local multiplet basis, *Phys. Rev. D* **103**, 094501 (2021).
- [102] A. N. Ciavarella and I. A. Chernyshev, Preparation of the SU(3) lattice Yang-Mills vacuum with variational quantum methods, *Phys. Rev. D* **105**, 074504 (2022).
- [103] S. A. Rahman, R. Lewis, E. Mendicelli, and S. Powell, SU(2) lattice gauge theory on a quantum annealer, *Phys. Rev. D* **104**, 034501 (2021).
- [104] M. Illa and M. J. Savage, Basic elements for simulations of standard-model physics with quantum annealers: Multigrid and clock states, *Phys. Rev. A* **106**, 052605 (2022).

- [105] A. Ciavarella, N. Klco, and M. J. Savage, Some conceptual aspects of operator design for quantum simulations of non-Abelian lattice gauge theories, [arXiv:2203.11988](#).
- [106] S. A. Rahman, R. Lewis, E. Mendicelli, and S. Powell, Self-mitigating Trotter circuits for SU(2) lattice gauge theory on a quantum computer, *Phys. Rev. D* **106**, 074502 (2022).
- [107] N. Klco and M. J. Savage, Systematically localizable operators for quantum simulations of quantum field theories, *Phys. Rev. A* **102**, 012619 (2020).
- [108] N. Klco and M. J. Savage, Fixed-point quantum circuits for quantum field theories, *Phys. Rev. A* **102**, 052422 (2020).
- [109] S. Wang, E. Fontana, M. Cerezo, K. Sharma, A. Sone, L. Cincio, and P. J. Coles, Noise-induced barren plateaus in variational quantum algorithms, *Nat. Commun.* **12**, 6961 (2021).
- [110] G. Scriva, N. Astrakhantsev, S. Pilati, and G. Mazzola, Challenges of variational quantum optimization with measurement shot noise, [arXiv:2308.00044](#).
- [111] H. R. Grimsley, S. E. Economou, E. Barnes, and N. J. Mayhall, An adaptive variational algorithm for exact molecular simulations on a quantum computer, *Nat. Commun.* **10**, eid 3007 (2019).
- [112] J. B. Kogut and L. Susskind, Hamiltonian formulation of Wilson’s lattice gauge theories, *Phys. Rev. D* **11**, 395 (1975).
- [113] T. Banks, L. Susskind, and J. B. Kogut, Strong coupling calculations of lattice gauge theories: (1+1)-dimensional exercises, *Phys. Rev. D* **13**, 1043 (1976).
- [114] R. Dempsey, I. R. Klebanov, S. S. Pufu, and B. Zan, Discrete chiral symmetry and mass shift in the lattice Hamiltonian approach to the Schwinger model, *Phys. Rev. Res.* **4**, 043133 (2022).
- [115] For faster convergence to the continuum, an $\mathcal{O}(a)$ improvement to the mass term can be performed to restore a discrete remnant of chiral symmetry in the $m \rightarrow 0$ limit [114].
- [116] The convention is that even fermion sites correspond to electrons, such that $\hat{Q}|\downarrow\rangle = 0$ and $\hat{Q}|\uparrow\rangle = -|\uparrow\rangle$, while the odd fermion sites correspond to positrons, such that $\hat{Q}|\uparrow\rangle = 0$ and $\hat{Q}|\downarrow\rangle = +|\downarrow\rangle$.
- [117] In the continuum, the chiral condensate is defined as $\chi_{\text{cont}} = \langle \bar{\psi} \psi \rangle$, which on the lattice becomes $\chi_{\text{lat}} = \frac{1}{L} \sum_j \langle \bar{\psi}_j \psi_j \rangle$, where j labels the spatial site. To have a positive quantity, we have added a constant to the definition of χ , $\chi \equiv \chi_{\text{lat}} + 1$. This counts the average number of electrons and positrons on a spatial site.
- [118] J. S. Van Dyke, K. Shirali, G. S. Barron, N. J. Mayhall, E. Barnes, and S. E. Economou, Scaling adaptive quantum simulation algorithms via operator pool tiling, [arXiv:2206.14215](#).
- [119] H. L. Tang, V. O. Shkolnikov, G. S. Barron, H. R. Grimsley, N. J. Mayhall, E. Barnes, and S. E. Economou, Qubit-ADAPT-VQE: An adaptive algorithm for constructing hardware-efficient Ansätze on a quantum processor, *PRX Quantum* **2**, eid 020310 (2021).
- [120] Y. S. Yordanov, C. H. W. Barnes, and D. R. M. Arvidsson-Shukur, Molecular-excited-state calculations with the qubit-excitation-based adaptive variational quantum eigensolver protocol, *Phys. Rev. A* **106**, 032434 (2022).
- [121] V. O. Shkolnikov, N. J. Mayhall, S. E. Economou, and E. Barnes, Avoiding symmetry roadblocks and minimizing the measurement overhead of adaptive variational quantum eigensolvers, *Quantum* **7**, 1040 (2023).
- [122] L. W. Bertels, H. R. Grimsley, S. E. Economou, E. Barnes, and N. J. Mayhall, Symmetry breaking slows convergence of the ADAPT variational quantum eigensolver, *J. Chem. Theor. Comput.* **18**, 6656 (2022).
- [123] P. G. Anastasiou, Y. Chen, N. J. Mayhall, E. Barnes, and S. E. Economou, TETRIS-ADAPT-VQE: An adaptive algorithm that yields shallower, denser circuit ansätze, [arXiv:2209.10562](#).
- [124] C. Feniou, M. Hassan, D. Traoré, E. Giner, Y. Maday, and J.-P. Piquemal, Overlap-ADAPT-VQE: Practical quantum chemistry on quantum computers via overlap-guided compact Ansätze, *Commun. Phys.* **6**, 192 (2023).
- [125] A. M. Romero, J. Engel, H. L. Tang, and S. E. Economou, Solving nuclear structure problems with the adaptive variational quantum algorithm, *Phys. Rev. C* **105**, 064317 (2022).
- [126] A. Pérez-Obiol, A. M. Romero, J. Menéndez, A. Rios, A. García-Sáez, and B. Juliá-Díaz, Nuclear shell-model simulation in digital quantum computers, *Sci. Rep.* **13**, 12291 (2023).
- [127] A. Peruzzo, J. McClean, P. Shadbolt, M.-H. Yung, X.-Q. Zhou, P. J. Love, A. Aspuru-Guzik, and J. L. O’Brien, A variational eigenvalue solver on a photonic quantum processor, *Nat. Commun.* **5**, eid 4213 (2014).
- [128] J. S. Bell, Time reversal in field theory, *Proc. Roy. Soc. Lond. A* **231**, 479 (1955).
- [129] J. S. Schwinger, The theory of quantized fields. 1., *Phys. Rev.* **82**, 914 (1951).
- [130] G. Luders, On the equivalence of invariance under time reversal and under particle-antiparticle conjugation for relativistic field theories, *Kong. Dan. Vid. Sel. Mat. Fys. Med.* **28N5**, 1 (1954).
- [131] In the total charge $Q = 0$ sector, there is a CP symmetry corresponding to the composition of a reflection through the midpoint of the lattice, exchanging *spatial* sites $n \leftrightarrow L - 1 - n$, and an interchange of an electron and a positron on each spatial site. In terms of spins on *staggered* sites, this is realized as $\hat{\sigma}_n^i \leftrightarrow \hat{\sigma}_{2L-1-n}^i$ followed by $\hat{\sigma}_n^i \leftrightarrow \hat{X}_n \hat{\sigma}_n^i \hat{X}_n$, where $\hat{\sigma}^i$ with $i = 1, 2, 3$ are the Pauli matrices. For example, under a CP transformation, the following $L = 4$ state becomes
- $$\begin{aligned} |\uparrow\downarrow\uparrow\uparrow\downarrow\downarrow\rangle &= |.. e^- e^+ e^+ e^- \rangle \\ &\xrightarrow{CP} |\downarrow\downarrow\uparrow\uparrow\downarrow\uparrow\rangle \\ &= |e^+ e^- .e^- e^+ . \rangle. \end{aligned} \quad (6)$$
- [132] An n -body operator involves n fermionic creation and n fermionic annihilation operators.
- [133] The commutators of $\hat{\Theta}$ operators not included in the pool are linear combinations of those that are in the pool.
- [134] For the range of m and g we have considered, it was necessary to consider only $\hat{\Theta}_m^S(d)$ with $d = 0, 1$ in the pool.

- Taking the continuum limit, where the correlation length diverges, will likely require keeping terms with $d > 1$.
- [135] R. J. Bartlett and M. Musiał, Coupled-cluster theory in quantum chemistry, *Rev. Mod. Phys.* **79**, 291 (2007).
- [136] G. Hagen, T. Papenbrock, M. Hjorth-Jensen, and D. J. Dean, Coupled-cluster computations of atomic nuclei, *Rep. Prog. Phys.* **77**, 096302 (2014).
- [137] IBM Quantum, 2023, <https://quantum-computing.ibm.com/>.
- [138] M. Treinish, *et al.*, Qiskit/qiskit-metapackage: Qiskit 0.43.3, 2023.
- [139] M. G. Algaba, P. V. Sriluckshmy, M. Leib, and F. Simkovic, Low-depth simulations of fermionic systems on square-grid quantum hardware, [arXiv:2302.01862](https://arxiv.org/abs/2302.01862).
- [140] These circuits have been verified by comparison with Trotterized exponentials of fermionic operators.
- [141] The staircase circuit can be modified into an X-shaped one, reducing the depth, but with the same number of CNOT gates [146].
- [142] The sixth and seventh steps were chosen for study in detail as the operator ordering has stabilized for $L \leq 14$. This allows the operator structure to be displayed in a single table, and enables the systematic extrapolation of parameters. The available classical computing resources limited the maximum number of steps of SC-ADAPT-VQE to ten.
- [143] The ordering of operators changes at $L = 10$ but the operator content is unchanged, so it is still possible to use $L = 8, 9$ in the extrapolation.
- [144] One could imagine generating the $\theta_i^{l=\infty}$ for a variety of m and g , and then machine-learning the variational parameters for all m and g . This could be particularly useful for m and g that approach the continuum limit, where the correlation length can no longer be contained within lattice volumes accessible to classical simulators.
- [145] The sixth operator in the extrapolation is a surface operator, whose contribution to the energy density scales as $1/L$. Therefore, if SC-ADAPT-VQE could be performed on, for example, $L = 500$, this operator would likely not be in the ansatz. Evidently the “error” introduced by extrapolating the ansatz with a surface operator is small since the deviation of observables for large L is the same as for $L \leq 14$.
- [146] A. Cowtan, S. Dilkes, R. Duncan, W. Simmons, and S. Sivarajah, Phase gadget synthesis for shallow circuits, *EPTCS* **318**, 213 (2020).
- [147] P. D. Nation, H. Kang, N. Sundaresan, and J. M. Gambetta, Scalable mitigation of measurement errors on quantum computers, *PRX Quantum* **2**, 040326 (2021).
- [148] L. Viola and S. Lloyd, Dynamical suppression of decoherence in two-state quantum systems, *Phys. Rev. A* **58**, 2733 (1998).
- [149] A. M. Souza, G. A. Álvarez, and D. Suter, Robust dynamical decoupling, *Philos. Trans. R. Soc.* **370**, 4748 (2012).
- [150] N. Ezzell, B. Pokharel, L. Tewala, G. Quiroz, and D. A. Lidar, Dynamical decoupling for superconducting qubits: a performance survey, [arXiv:2207.03670](https://arxiv.org/abs/2207.03670).
- [151] M. Urbanek, B. Nachman, V. R. Pascuzzi, A. He, C. W. Bauer, and W. A. de Jong, Mitigating depolarizing noise on quantum computers with noise-estimation circuits, *Phys. Rev. Lett.* **127**, 270502 (2021).
- [152] J. J. Wallman and J. Emerson, Noise tailoring for scalable quantum computation via randomized compiling, *Phys. Rev. A* **94**, 052325 (2016).
- [153] For all of the results presented in this work, correlated bootstrap resampling was used to estimate statistical (shot) uncertainties. The circuits used for $L \leq 40$ were executed on `ibm_brisbane` with 40 Pauli-twirled instances for both the mitigation and the physics circuits, each with 8×10^3 shots. For $L = 50$, the M3 method was not applied due to the large overhead in classical computing, and production was executed on `ibm_cusco` with 150 Pauli-twirled instances. Additional details can be found in Appendix G.
- [154] N. Klco and M. J. Savage, Minimally entangled state preparation of localized wave functions on quantum computers, *Phys. Rev. A* **102**, 012612 (2020).
- [155] H. Yu, Y. Zhao, and T.-C. Wei, Simulating large-size quantum spin chains on cloud-based superconducting quantum computers, *Phys. Rev. Res.* **5**, 013183 (2023).
- [156] Y. Kim, A. Eddins, S. Anand, K. X. Wei, E. van den Berg, S. Rosenblatt, H. Nayfeh, Y. Wu, M. Zaletel, K. Temme, and A. Kandala, Evidence for the utility of quantum computing before fault tolerance, *Nature* **618**, 500 (2023).
- [157] O. Shtanko, D. S. Wang, H. Zhang, N. Harle, A. Seif, R. Movassagh, and Z. Mineev, Uncovering local integrability in quantum many-body dynamics, [arXiv:2307.07552](https://arxiv.org/abs/2307.07552).
- [158] For periodic boundary conditions, $\langle \hat{Q}_k \rangle = 0$, but for OBCs $\langle \hat{Q}_k \rangle$ decays exponentially away from the boundaries; see Appendix B.
- [159] The exponential decay of charge-charge correlations provides motivation for the construction of a truncated Hamiltonian where charge-charge terms are omitted beyond a certain distance. See Appendix A for more details.
- [160] R. Verdel, F. Liu, S. Whitsitt, A. V. Gorshkov, and M. Heyl, Real-time dynamics of string breaking in quantum spin chains, *Phys. Rev. B* **102**, 014308 (2020).
- [161] A. Milsted, J. Liu, J. Preskill, and G. Vidal, Collisions of false-vacuum bubble walls in a quantum spin chain, *PRX Quantum* **3**, 020316 (2022).
- [162] Wolfram Research, Inc., Mathematica, version 13.0.1, 2022, Champaign, IL. <https://www.wolfram.com/mathematica>.
- [163] G. Van Rossum and F. L. Drake, *Python 3 Reference Manual* (CreateSpace, Scotts Valley, CA, 2009).
- [164] J. D. Hunter, Matplotlib: A 2D graphics environment, *Comput. Sci. Eng.* **9**, 90 (2007).
- [165] J. Bezanson, A. Edelman, S. Karpinski, and V. B. Shah, Julia: A fresh approach to numerical computing, *SIAM Rev.* **59**, 65 (2017).
- [166] F. Pérez and B. E. Granger, IPython: A system for interactive scientific computing, *Comput. Sci. Eng.* **9**, 21 (2007).
- [167] Anaconda Inc., Anaconda Software Distribution, version 2-2.4.0, 2020, <https://docs.anaconda.com/>.
- [168] M. Fishman, S. R. White, and E. M. Stoudenmire, The ITensor software library for tensor network calculations, *SciPost Phys. Codebases* **4** (2022).

- [169] For the current paper, because of the small number of parameters, the selection of the points to be fitted was determined by visual inspection (if the points followed an exponential decay or did not).
- [170] C. Michael, Adjoint sources in lattice gauge theory, *Nucl. Phys. B* **259**, 58 (1985).
- [171] M. Lüscher and U. Wolff, How to calculate the elastic scattering matrix in two-dimensional quantum field theories by numerical simulation, *Nucl. Phys. B* **339**, 222 (1990).
- [172] T. A. DeGrand and D. Toussaint, From Actions to Answers: Proceedings of the 1989 Theoretical Advanced Study Institute in Elementary Particle Physics, 5-30 June, 1989, University of Colorado, Boulder (1990).
- [173] G. T. Fleming, in *QCD and Numerical Analysis III. Lecture Notes in Computational Science and Engineering*, edited by A. Boriç, A. Frommer, B. Joó, A. Kennedy, and B. Pendleton, Vol. 47 (Springer, Berlin, Heidelberg, 2005).
- [174] S. R. Beane, W. Detmold, T. C. Luu, K. Orginos, A. Parreño, M. J. Savage, A. Torok, and A. Walker-Loud, High statistics analysis using anisotropic clover lattices: Single hadron correlation functions, *Phys. Rev. D* **79**, 114502 (2009).
- [175] W. Dür, M. Hein, J. I. Cirac, and H.-J. Briegel, Standard forms of noisy quantum operations via depolarization, *Phys. Rev. A* **72**, 052326 (2005).
- [176] This is not true for observables involving the entire qubit register, e.g., the vacuum-vacuum persistence probability. This is because applying the $Q = 0$ constraint when one is measuring global observables will not introduce any new correlations.
- [177] Qiskit Aer 12.0 MPS documentation, 2023, https://qiskit.org/ecosystem/aer/tutorials/7_matrix_product_state_method.html.
- [178] Y. Li and S. C. Benjamin, Efficient variational quantum simulator incorporating active error minimization, *Phys. Rev. X* **7**, 021050 (2017).
- [179] K. Temme, S. Bravyi, and J. M. Gambetta, Error mitigation for short-depth quantum circuits, *Phys. Rev. Lett.* **119**, 180509 (2017).
- [180] T. Giurgica-Tiron, Y. Hindy, R. LaRose, A. Mari, and W. J. Zeng, in *2020 IEEE International Conference on Quantum Computing and Engineering (QCE)* (IEEE, Denver, 2020), p. 306.
- [181] E. van den Berg, Z. K. Mineev, A. Kandala, and K. Temme, Probabilistic error cancellation with sparse Pauli-Lindblad models on noisy quantum processors, *Nat. Phys.* **19**, 1116 (2023).
- [182] Kevin J. Sung, Nick Bronn, Dariusz Lasecki, George Zhou, A. J. Rasmusson, and Jim Garrison, “qiskit-research/qiskit-research: Version 0.0.1”, 2023.